HYDRODYNAMIC ANALYSIS OF UNDERWATER BODIES FOR EFFICIENT STATION KEEPING IN SHALLOW WATERS WITH SURFACE WAVES

by

Matthew Bradley

A Thesis Submitted to the Faculty of

The College of Engineering and Computer Science

In Partial Fulfillment of the Requirements for the Degree of

Master of Science

Florida Atlantic University

Boca Raton, Florida

May 2014

HYDRODYNAMIC ANALYSIS OF UNDERWATER BODIES FOR EFFICIENT

STATION KEEPNG IN SHALLOW WATERS WITH SURFACE WAVES

by

Matthew Bradley

This thesis was prepared under the direction of the candidate's thesis advisor, Dr. P. Ananthakrishnan, Department of Ocean and Mechanical Engineering, and has been approved by the members of his supervisory committee. It was submitted to the faculty of the College of Engineering and Computer Science and was accepted in partial fulfillment of the requirements for the degree of Master of Science.

SUPERVISORY COMMITTEE:

P. Ananthakrishnan, Ph.D.
Thesis Advisor

Manhar Dhanak, Ph.D.

Edgar An, Ph.D.

Javad Hashemi, Ph.D.
Chair, Department of Ocean and Mechanical Engineering

Mohammad Ilyas, Ph.D.
Dean, College of Engineering and Computer Science

Deborah L. Floyd, Ed.D.
Interim Dean, Graduate College

3/25/14
Date

ACKNOWLEDGEMENTS

I would like to thank my thesis advisor Dr. P. Ananthakrishnan for providing insight and guidance throughout my undergraduate and graduate career and specifically with the development and preparation of this thesis. In addition, I would like to thank my thesis committee members, Dr. Manhar Dhanak and Dr. Edgar An for their encouragement to pursue graduate studies and their comments and advice on this research project. I would also like to thank Dr. Mark Hyman of the Naval Surface Warfare Center (NSWC) Panama City Division for insightful comments and discussions on the project. Finally I would like to thank the faculty and staff of the Department of Ocean and Mechanical Engineering for providing an astounding environment in which to complete my undergraduate and graduate studies.

Financial support in the form of graduate research assistantship provided by the US Office of Naval Research (ONR) through the Naval Engineering Education Consortium led by the University of Michigan at Ann Arbor is gratefully acknowledged.

I would like to thank my family and friends for their loving support throughout my graduate career. Your encouragement and advice has helped me achieve so many of my life goals.

ABSTRACT

Author:	Matthew Bradley
Title:	Hydrodynamic Analysis of Underwater Bodies for Efficient Station Keeping in Shallow Waters with Surface Waves
Institution:	Florida Atlantic University
Thesis Advisor:	Dr. Palaniswamy Ananthakrishnan
Degree:	Master of Science
Year:	2014

To determine the effect of body shape on the response of underwater vehicles to surface waves in shallow water, the wave radiation hydrodynamic forces are evaluated for a family of (i) prolate spheroidal hull forms and (ii) cylindrical bodies with hemispherical nose and conical tail sections by systematically varying the geometric parameters but keeping displacement constant. The added-mass and wave damping coefficients are determined using a frequency-domain, simple-source based boundary integral method. Results are obtained for a range of wave frequencies and depths of vehicle submergence all for a fixed water depth of 10 m. With the wave exciting force and moment determined using the Froude-Krylov theory, the response transfer functions for heave and pitch are then determined. The heave and pitch response spectra in actual littoral seas are then determined with the sea state modeled using TMA spectral relations. Results show that vehicle slenderness is a key factor affecting the hydrodynamic

coefficients and response. The results show two characteristics that increase the radiation hydrodynamic forces corresponding to heave and pitch motions: namely, vehicle length and further-away from mid-vehicle location of the body shoulder. The opposite is true for the oscillatory surge motion. By utilizing these observed characteristics, one can design the lines for maximum radiation forces and consequently minimum hull response for the critical modes of rigid-body motion in given waters and vehicle missions. In the studies carried out in the thesis, a hull with a long parallel middle body with hemispherical nose and conical tail sections has better heave and pitch response characteristics compared prolate spheroid geometry of same volume. The methodology developed herein, which is computationally efficient, can be used to determine optimal hull geometry for minimal passive vehicle response in a given sea.

HYDRODYNAMIC ANALYSIS OF UNDERWATER BODIES FOR EFFICIENT STATION KEEPING IN SHALLOW WATERS WITH SURFACE WAVES

LIST OF TABLES

LIST OF FIGURES

CHAPTER 1: INTRODUCTION

Chapter 1 begins by describing various underwater vehicles and observation platforms, their benefits and how this project is expected to contribute to improving their design and performance efficiency. The second part of this chapter discusses past research that is related to this thesis, followed by the discussion of the formulations and solution techniques used for station-keeping of underwater bodies. Finally, the objectives and scope of the thesis are presented.

1.1 Underwater Vehicles

The design and use of autonomous underwater vehicles (AUV) began in the 1960's with the development of the vehicle Sea Spook [50]. These vehicles were developed for ocean measurements, surveillance and payload delivery for commercial and defense applications. Other vehicle uses include routine maintenance of underwater structures and vessels as well as repairs in places inaccessible to humans. Development continued through the 1970s and 1980s but with more rapid technological and communication related advancements in the 90s, the improvements to AUV design have increased rapidly. These developments and advancements have led to their use in both littoral and deeper waters without unnecessary risk of human life. The real challenge to the design of an underwater vehicle is the adaptation to different sea state conditions either to maintain its position or to maneuver. The problem of maintaining position or

dynamic stability is further compounded when underwater vehicles operate at a depth where the effect of surface waves can be significant [51].

1.2 Works Related to this Thesis:

In literature, one can find ample works on the effect of body shapes on the hydrodynamic performance of marine vehicles both for floating and submerged bodies. Focusing on floating ships first, in the works of Tuck [56], Vanden-Broeck and Tuck [57], and Wehausen [65], based on the linear potential wave theory, *wave-less* body shapes having zero wave resistance were identified. In Grosenbaugh and Yeung [20] and Yeung [66] the effect of a bulbous bow of a ship on the wave radiation resistance was examined including the free surface nonlinearity. In the classical work of Ursell [61], it was shown that per linear theory the reflection of waves over a submerged cylinder of circular cross section is zero. Kim [30] studied radiation hydrodynamic characteristics of half-immersed ellipsoidal body shapes for a range of frequencies in *infinitely deep water*. Focusing on the body motions of heave, surge, and pitch, Kim varied the aspect ratio (body length to body diameter) of the ellipsoidal body, each shape with a different displaced volume, and analyzed the hydrodynamic coefficients. The results showed diminishing hydrodynamic coefficients as the body shape changed from aspect ratio 1/1 (sphere) to ratio 8/1 for surge, heave, and pitch motions. Although not specifically stated in his work, these results may be affiliated with the diminishing surface area as the aspect ratio decreases from 1/1 to 8/1.

On the subject of submerged bodies, Taylor and Wu [54] analyzed the wave radiation and diffraction problem of submerged ellipsoids in *infinitely deep* water. Utilizing three-dimensional linearized potential flow theory and appropriate fluid domain

boundary conditions, Taylor and Wu calculated the 6 Degree of Freedom (DOF) hydrodynamic coefficients for ellipsoids of various aspect ratios submerged at a depth below the sea surface of twice the minor axis radius. Differing from the work of Kim, Taylor and Wu maintain constant displaced volume for all aspect ratios studied. For surge motion, results show that the smallest hydrodynamic coefficients correspond to the body with the smallest aspect ratio (6/1) while the smallest coefficients for heave motion correspond to the largest aspect ratio (4/1). For pitch motion, the smallest hydrodynamic coefficients correspond to the shortest overall body length (aspect ratio 4/1). These results show that a particular aspect ratio does not minimize or maximize these hydrodynamic coefficients for all modes of motion.

In the works discussed previously, the effect of body shape on the hydrodynamic coefficients has been studied for both floating and submerged bodies. However, to the best of the author's knowledge not much work, if any has been carried out on the effect of body shape on the motion response to *waves*. Perhaps this has not yet been studied because the motion response of a body, for a given shape, will depend on the forces of not only the incident wave but also on diffracted and radiated waves and hence analytical determination of the shape effect to body waves is intractable. Only for simple shapes of course there are theories such as the Haskind relation relating wave exciting and damping forces [43]. Since the knowledge of the body shape effect on the motion response to surface waves will greatly enhance the passive station keeping of underwater platforms, a computational study to determine the effect for a family of shapes and range of parameters is pursued in this thesis. Starting from a parent hull, the principal parameters are systematically varied to identify the key parameters affecting the response. Two

parent hulls, one of prolate spheroid and the other of a circular cylinder with hemispherical nose and conical tail sections, are considered in this thesis.

1.3 Computational Hydrodynamic Theories

Few works have been carried out theoretically which aid in the practical design of ships. A classic example is the thin-ship theory of Michell which was derived in 1800's but to this day is used to determine the wave resistance of fast ships [41]. Tools for most practical or nonlinear ship hydrodynamics problems are based on numerical methods. As for example, the boundary integral method based on simple-source distribution developed by Yeung [67] can be used to study *linear* radiation hydrodynamics of arbitrary bodies in waters with arbitrary bathymetry. Fully nonlinear time-domain analysis has been made possible by the mixed Eulerian-Lagrangian formulation based boundary-integral method developed by Longuet-Higgins and Cokelet [36]. Considerable progress has been made in the development of computational methods for nonlinear wave-body interactions including effects of viscosity. These methods can be grouped into categories of volume of fluid method (Hirt and Nichols [21] and Miyata [42]), boundary-fitted coordinates method (Ananthakrishnan [6]), level-set method (Vogt and Kang [62]) and smoothed particle hydrodynamics method (Gomez-Gesteira and Dalrymple [19]). In the present thesis, only the inviscid effect of the body shape is considered on the motion response and radiation hydrodynamic forces. Consideration of viscosity effect could be a future effort. For inviscid wave-body interaction problems, boundary-integral methods are more attractive particularly because of their ability to track the free surface and computational efficiency. In the present work, boundary integral methods based on the potential flow

theory are used to study the effect of body shapes on the hydrodynamic forces and body response to waves in the frequency domain for the linear case.

1.4 Scope of Thesis

The purpose of this thesis is to determine the effect of underwater vehicle shapes on the motion response to waves in shallow waters. The research is based on a boundary integral method algorithm that is developed as part of the thesis effort. The original contribution of the thesis is identification of principle geometric parameters and shapes affecting or minimizing motion response of underwater bodies in shallow water wave fields and a development of an algorithm and methodology to determine the hydrodynamic coefficients and response of underwater bodies in shallow waters. In order to demonstrate the methodology, two families of hull forms are studied at various depths of body submergence with body parameters varied systematically all within a fixed and constant water depth. A spheroid hull form acts as a parent hull for the first family and from this, the aspect ratio (body length to body diameter) is altered while maintaining constant body displacement. For the second parent hull form, a body consisting of a parallel mid-body with a hemispheric nose cone and conical tail is studied. From this form, the parallel mid-body aspect ratio is altered while maintaining constant body displacement. Utilizing the same values for body volume, water depth and depth of body submergence in the analysis of both hull forms allows for accurate comparisons and conclusions. In each case, the radiation force is calculated from the hydrodynamic coefficients, followed by using the incident, diffracted, and radiated wave forces to calculate the transfer functions for surge, heave, and pitch motions of the body over a range of frequency values. Finally, the body response spectra are determined for various

sea state conditions by combining the transfer functions with seas modeled using shallow water TMA spectral relation [22].

Thus the goal of the computational study is to determine body-shape effects on the incident and radiated wave forces and subsequently the motion response. The knowledge will serve to identify optimum shapes from the viewpoint of efficient station keeping in wave energetic coastal waters.

CHAPTER 2: FORMULATION OF WAVE MOTION PROBLEM USING POTENTIAL THEORY

In chapter 2, we begin by introducing potential theory and presenting the governing equations for the wave-body interaction problem. Next, we define the submerged body and the fluid boundaries. After defining each boundary, the appropriate boundary equations are presented and are later used in the interaction problem.

2.1 Potential Theory

Neglecting fluid viscosity and assuming flow to be incompressible and irrotational [14], one obtains the following potential-flow equations for a wave-body interaction problem:

$$\vec{u} = \nabla\phi \tag{2.1}$$

and

$$\nabla^2\phi = 0 \tag{2.2}$$

where $\vec{u}$ is the fluid velocity vector and ϕ is the gradient of a scalar potential, known as the velocity potential. The second equation is known as the Laplace Equation which governs the analysis throughout this thesis. A relationship between velocity potential and gage pressure is obtained by substituting the definition of the velocity potential into Euler's equation and integrating with respect to space. This relationship is defined below:

$$p = -\rho \frac{\partial \phi}{\partial t} - \frac{\rho}{2} |\nabla \phi|^2 - \rho g z \tag{2.3}$$

where p is the gage pressure, the difference between atmospheric pressure and absolute pressure, ρ the fluid density, and g the gravity constant. Next, we utilize the above hydrodynamic relationships to determine boundary equations for a wave-body interaction problem.

2.2 Formulation of Wave-Body Interaction Problem

The first step in solving the wave-body interaction problem is the determination of fluid and body boundaries and their respective conditions. Suppose a three dimensional fluid domain is bounded by the sea surface boundary *F*, sea floor boundary *B*, and a far-field boundary Σ, which all encompass a submerged body boundary *H*, as shown in Figure 2-1. Note that in Figure 2-1 the coordinate system is modeled using Cartesian coordinates with the positive *z*-axis pointing in the vertical direction, the positive *x*-axis to the right and the positive *y*-axis pointing into the page. The origin (*0,0,0*) is located on the calm free surface directly above the center of the submerged body *H* and the center of the submerged body has coordinates (*0,0,-h*) where *h* is the submergence depth of the vehicle.

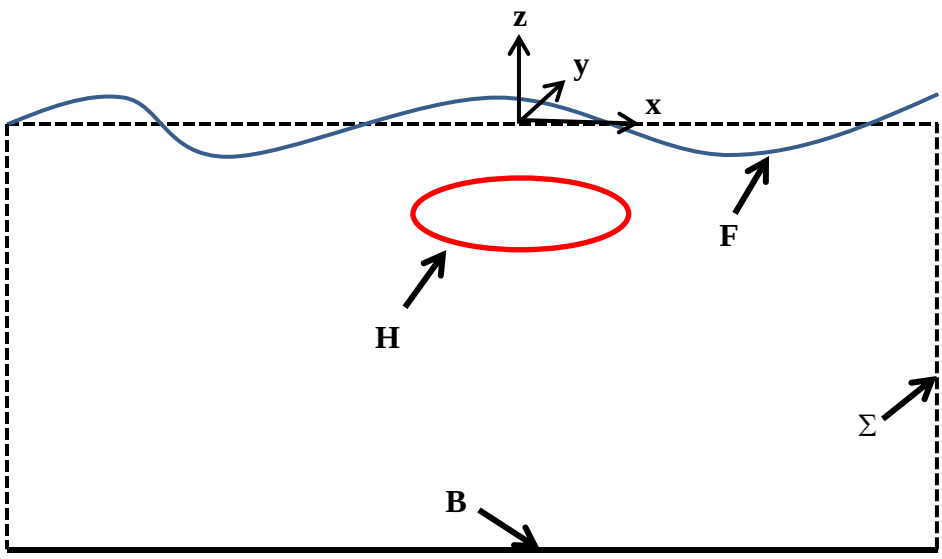

Figure 2-1: Fluid domain surrounding submerged body

2.2.1 Body with Free Surface Effects

If the body is near the free surface, an equation must be used to model the free surface. We utilize two conditions for the sea surface boundary, namely the dynamic and kinematic free-surface boundary conditions. To formulate these equations, we first assume that the boundary at the surface between water and air is a material boundary [14]. Let the free surface be defined as

$$F(x, y, z, t) = z - \eta(x, y, t) = 0 \tag{2.4}$$

Here, F is the particle position as a function of space and time, η is the wave elevation as a function of position and time and z represents the vertical distance from the mean sea surface. Since the boundary is material, any fluid particle moves with the surface, therefore we set the total time derivative to zero:

$$\frac{DF(x, y, z, t)}{Dt} = \frac{\partial F}{\partial t} + u\frac{\partial F}{\partial x} + v\frac{\partial F}{\partial y} + w\frac{\partial F}{\partial z} = 0 \tag{2.5}$$

where (u,v,w) represent the (x,y,z) vector components of velocity $\vec{u}$. Using the definition from equation (2.4) and substituting, equation (2.5) becomes:

$$-\frac{\partial \eta}{\partial t}-\frac{\partial \phi}{\partial x}\frac{\partial \eta}{\partial x}-\frac{\partial \phi}{\partial y}\frac{\partial \eta}{\partial y}+\frac{\partial \phi}{\partial z}=0 \quad \text{on the free surface } (F) \tag{2.6}$$

which is known as the kinematic free-surface boundary condition. The second condition is based on the dynamics of the surface. Without viscosity and surface tension, gage pressure must be zero on the free surface:

$$P_{gage}=P_{absolute}-P_{atmosphere}=0 \tag{2.7}$$

Substituting into Euler's integral gives,

$$p_{gage}=0=-\rho\frac{\partial \phi}{\partial t}-\frac{\rho}{2}\left|\nabla\phi\right|^2-\rho g z \quad \text{on z = } \eta$$

$$\frac{\partial \phi}{\partial t}+\frac{1}{2}\left|\nabla\phi\right|^2+g\eta=0 \text{ on the free surface } (F) \tag{2.8}$$

where z = η on the free surface. Equation (2.8) represents the dynamic free-surface boundary condition.

2.2.2 Body with Sea Floor Effects

For a body submerged close to the sea floor, we must include these effects and therefore set a condition for no flux of fluid across the sea floor. The following equation represents the boundary condition

$$\frac{\partial \phi}{\partial n}=0 \quad \text{on the sea floor } (B) \tag{2.9}$$

2.3 Linearization

The free surface conditions above are in non-linear form. However, for a body undergoing small amplitude motion, non-linear effects are minimal and are ignored which allow linearization of these boundary conditions. In the case of small-amplitude waves (i.e., wave height smaller than the wave length) the velocity potential, wave elevation and all their derivatives are small. So to the leading order, the linearized boundary conditions become:

$$-\frac{\partial \eta}{\partial t}-\cancel{\frac{\partial \phi}{\partial x}\frac{\partial \eta}{\partial x}}-\cancel{\frac{\partial \phi}{\partial y}\frac{\partial \eta}{\partial y}}+\frac{\partial \phi}{\partial z}=0 \rightarrow -\frac{\partial \eta}{\partial t}+\frac{\partial \phi}{\partial z}=0 \tag{2.10}$$

$$\frac{\partial \phi}{\partial t}+\cancel{\frac{1}{2}|\nabla \phi|^2}+g\eta=0 \rightarrow \frac{\partial \phi}{\partial t}+g\eta=0 \tag{2.11}$$

Consistent with the linearization, the above conditions are to be imposed on the calm surface z = 0 [14]. Above equations are referred to as the linearized kinematic and dynamic free-surface conditions. These equations can be combined by eliminating η to obtain the following linearized combined free-surface condition:

$$\frac{\partial^2 \phi}{\partial t^2}+g\frac{\partial \phi}{\partial z}=0 \tag{2.12}$$

When the body is submerged close to the free surface, a condition for the far-field boundary is needed. In the work of Yeung [67], he presents the radiation condition which is applied at a finite distance from the origin.

$$\frac{\partial \phi}{\partial R}=\left(-\frac{1}{2R}+i^* k\right)\phi \tag{2.13}$$

where R is the horizontal distance from the origin, i^* the imaginary unit, and k the corresponding wave number. Next, we focus on using Green's theorem to derive the wave-body interaction equation.

CHAPTER 3: BOUNDARY INTEGRAL METHOD

In this chapter, we begin by presenting Green's Theorem and formulate a surface integral equation for an arbitrary fluid flow. Next, we apply the formulation to the fluid domain described in Chapter 2 and apply the boundary conditions formulated previously. At the end of this chapter, two wave-body interaction surface integrals are presented, namely the linearized frequency domain wave-body interaction integral and the non-linear time domain wave-body interaction integral.

3.1 Green's Theorem

This theorem is a critical step in the process to derive the wave-body interaction equation. First, we start with an arbitrary flow or a volume of fluid as seen in figure 3-1.

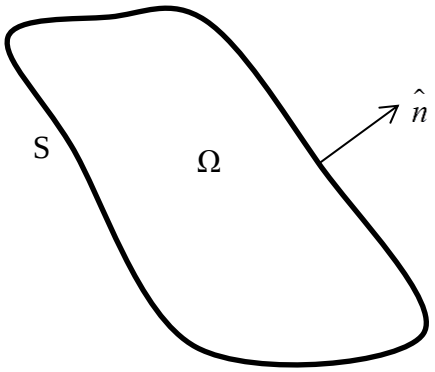

Figure 3-1: Volume of a fluid

In this figure, S is the surface of the fluid, Ω the domain of the fluid, and n is the normal vector pointing out of the fluid. Letting $\vec{A}$ represent a vector-field quantity within the above flow, we use Green's First Identity to show a relationship between a volumetric

integral and surface integral. This identity is also known as the Divergence or Gauss Theorem [43] and states:

$$\int_{\Omega} \nabla \cdot \vec{A}\, d\Omega = \int_{S} \vec{A} \cdot \hat{n}\, dS \tag{3.1}$$

where $\nabla \cdot \vec{A}$ is the divergence of the vector $\vec{A}$, and $d\Omega$ and dS represent the differential volume and differential area respectively. If ϕ and G are scalar functions defined in the fluid domain Ω, we set $\vec{A} = \phi \nabla G$ and $\vec{A} = G \nabla \phi$. Substituting both definitions of $\vec{A}$ into equation (3.1), we obtain two equations:

$$\begin{aligned} \int_{\Omega} \left(\nabla \phi \cdot \nabla G + \phi \nabla^2 G \right) d\Omega &= \int_{S} \phi \frac{\partial G}{\partial n} dS \\ \int_{\Omega} \left(\nabla G \cdot \nabla \phi + G \nabla^2 \phi \right) d\Omega &= \int_{S} G \frac{\partial \phi}{\partial n} dS \end{aligned} \tag{3.2}$$

Subtracting the two equations above leads to the following relationship:

$$\int_{\Omega} \left(\phi \nabla^2 G - G \nabla^2 \phi \right) d\Omega = \int_{S} \left(\phi \frac{\partial G}{\partial n} - G \frac{\partial \phi}{\partial n} \right) dS \tag{3.3}$$

Since both ϕ and G satisfy the Laplace Equation, then in equation (3.3), $\nabla^2 G = 0$ and $\nabla^2 \phi = 0$. Upon simplification, only the surface integral remains:

$$\int_{S} \left(\phi \frac{\partial G}{\partial n} - G \frac{\partial \phi}{\partial n} \right) dS = 0 \tag{3.4}$$

Equation (3.4) is commonly referred to as Green's Second Identity and note that this equation involves only a surface integral. The next step in Green's theorem is solving for the function G. To achieve this, let $\vec{P}(x, y, z)$ represent a field point within the three dimensional fluid domain and $\vec{Q}(\xi, \eta, \zeta)$ represent a source point within the same fluid domain where the distance between P and Q is set to:

$$r = \sqrt{(x-\xi)^2 + (y-\eta)^2 + (z-\zeta)^2} \tag{3.5}$$

Allow *G* to represent the potential due to the point source except when the source point and field point coincide. With these assumptions, the solution to the Green's function is $G = -\frac{1}{r}$. However, when the source panel and field panel coincide the distance between *P* and *Q* is zero ($r = 0$) and substituting into the Green's function $-\frac{1}{r}$ creates a singularity. To rectify this, a small sphere of fluid is placed within the fluid domain Ω surrounding the field point *P*. A two dimensional rendering is seen in Figure 3-2.

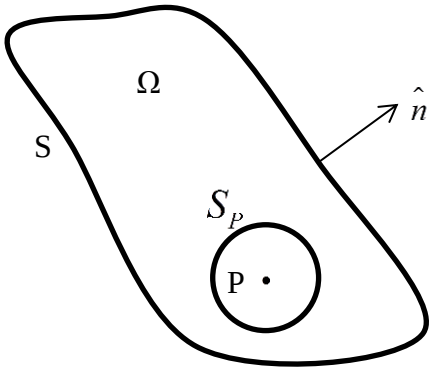

Figure 3-2: Fluid volume for singularity rectification

Here, S_P represents the surface of the fluid volume enclosing the field point *P*. By applying equation (3.4) to the new fluid volume shown in Figure 3-2, the following relationship is derived:

$$\int_S \left(\phi \frac{\partial G}{\partial n} - G \frac{\partial \phi}{\partial n} \right) dS - \int_{S_P} \left(\phi \frac{\partial G}{\partial n} - G \frac{\partial \phi}{\partial n} \right) dS_P = 0 \tag{3.6}$$

Taking the limit as the radius of the sphere $r_P \to 0$ the second integral from equation (3.6) simplifies to $4\pi\phi(\mathrm{P})$ when *P* is within the fluid as seen in figure 3-2. For cases when the particle *P* is on the boundary, the sphere S_P needs only to be a hemisphere and

equation (3.6) simplifies to $2\pi\phi(P)$ [43]. These two possible locations of point *P* yield two equations for the three-dimensional wave body interaction problem presented in equation (3.7).

$$\begin{matrix} 2\pi\phi(P) \\ 4\pi\phi(P) \end{matrix}\Bigg| + \int_S \phi \frac{\partial}{\partial n}\frac{1}{r} dS = \int_S \frac{1}{r}\frac{\partial \phi}{\partial n} dS \Bigg| \begin{matrix} \text{for P on the boundary} \\ \text{for P within the boundary} \end{matrix} \tag{3.7}$$

In the case of this thesis, we are only interested in the potential when the field point *P* rests on the fluid boundary and therefore $2\pi\phi(P)$ is used. With the general equation derived, in the next section we relate and substitute the body and fluid boundaries for the surface integral *S*.

3.2 Application of Green's Theorem

In this section, Green's Theorem is applied to the wave-body interaction problem formulated in Chapter 2 and illustrated in Figure 3-3 below.

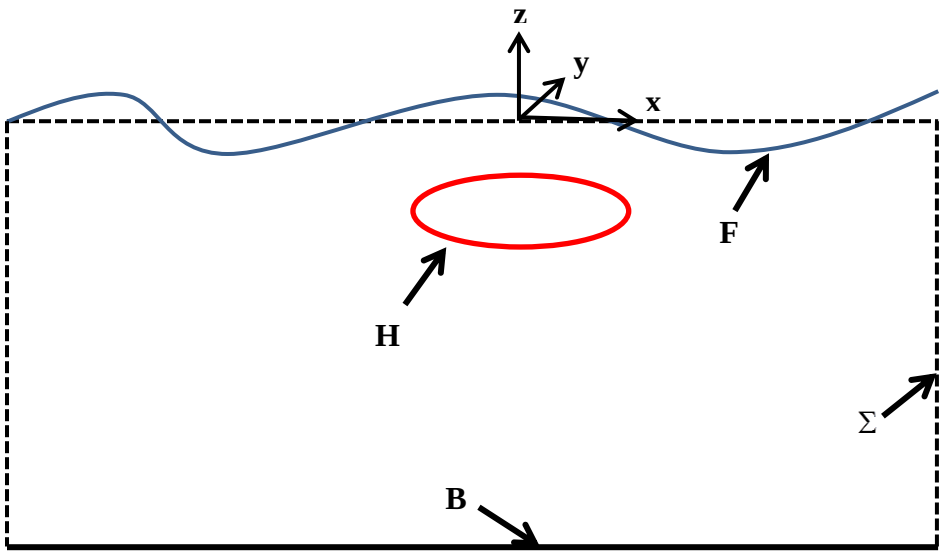

Figure 3-3: Fluid domain surrounding submerged body

3.2.1 Linear Frequency Domain Analysis for Wave-Body Interactions

The following formulation follows the Ph.D. work of Yeung [63]. Reader may therefore refer to Yeung [63] for details. For a body in shallow waters with surface effects, the linearized boundary condition equations for potential flow in an incompressible, irrotational, and inviscid fluid are given by:

$\nabla^2\phi = 0$ in the fluid domain Ω

$\frac{\partial\phi}{\partial n} = V \cdot n$ on the body surface H

$\frac{\partial\phi}{\partial n} = 0$ on the sea floor boundary B

$\frac{\partial^2\phi}{\partial t^2} + g\frac{\partial\phi}{\partial n} = 0$ on the sea surface F

$\frac{\partial\phi}{\partial R} = \left(-\frac{1}{2R} + i^* k\right)\phi$ on the far-field boundary Σ

We set the body motion in the following form.

$$\alpha_j = \mathrm{Re}\left(A_j e^{-i^*\sigma t}\right) \tag{3.8}$$

In equation (3.8), i^* is the imaginary unit $\sqrt{-1}$, σ the angular frequency of oscillation, t the time variable, A_j the motion amplitude, j the mode of motion, and α_j the real part of the variable. Based on the Cartesian coordinate system developed in Chapter 2, the variable j represents the six degrees of freedom of motion and is assigned the following set of values:

$1 \rightarrow$ surge

$2 \rightarrow$ sway

$3 \rightarrow$ heave

$4 \rightarrow$ roll

$5 \rightarrow$ pitch

$6 \rightarrow$ yaw

Since the problem is linear, the corresponding velocity potential can be written as:

$$\phi = Ae^{-i^* \sigma t} \tag{3.9}$$

Substituting in the governing equations, we get:

$\nabla^2 \phi_j = 0$ in the fluid domain Ω

$\frac{\partial \phi_j}{\partial n} = \hat{n}_j$ on the body surface H

$\frac{\partial \phi_j}{\partial n} = 0$ on the sea floor boundary B

$\frac{\partial \phi_j}{\partial n} - \frac{\sigma^2}{g} \phi_j = 0$ on the sea surface F

$\frac{\partial \phi_j}{\partial R} - \left(-\frac{1}{2R} + i^* k \right) \frac{1}{r} \phi_j = 0$ on the far-field boundary Σ

In the above conditions, k represents the wave number, ϕ_j the velocity potential for the j^{th} mode of motion, R is the horizontal distance from the origin, r the three-dimensional distance between the source and field point, and $\hat{n}_j$ is the normal vector corresponding to the body's mode of motion which per Kirchhoff's (modal) decomposition [43] are given by:

$$\hat{n}_j = \begin{cases} \hat{n}_j & \text{for j =1,2,3} \\ (\vec{r} \times \hat{n}_{j-3}) & \text{for j = 4,5,6} \end{cases}$$

The wave number k is derived using the full dispersion relation of $\sigma^2 = gk\tanh(kh)$ where h is the water depth. Substituting these frequency domain boundary conditions into Green's Theorem equation (3.6), we achieve the following:

$$\begin{aligned} &2\pi\phi_j(P) + \int_H \phi_j \frac{\partial}{\partial n}\frac{1}{r} dH + \int_B \phi_j \frac{\partial}{\partial n}\frac{1}{r} dB + \int_F \phi_j \frac{\partial}{\partial n}\frac{1}{r} dF + \int_\Sigma \phi_j \frac{\partial}{\partial n}\frac{1}{r} d\Sigma \\ &= \int_H \frac{\hat{n}_j}{r} dH + \int_F \phi_j \frac{\sigma^2}{g}\frac{1}{r} dF + \int_\Sigma \phi_j \left(-\frac{1}{2R} + i^* k\right)\frac{1}{r} d\Sigma \end{aligned} \tag{3.10}$$

With known integrals moved to the right hand side of the equation and the unknown quantities to the left hand side, equation (3.10) becomes:

$$\begin{aligned} &2\pi\phi_j(P) + \int_H \phi_j \frac{\partial}{\partial n}\frac{1}{r} dH + \int_B \phi_j \frac{\partial}{\partial n}\frac{1}{r} dB + \int_F \phi_j \left[\frac{\partial}{\partial n}\frac{1}{r} - \frac{\sigma^2}{g}\frac{1}{r}\right] dF \\ &+ \int_\Sigma \phi_j \left[\frac{\partial}{\partial n}\frac{1}{r} - \left(-\frac{1}{2R} + i^* k\right)\frac{1}{r}\right] d\Sigma = \int_H \frac{\hat{n}_j}{r} dH \end{aligned} \tag{3.11}$$

Solving equation (3.11) for the unknown variable yields the solution to the velocity potential on every surface for the j^{th} mode of motion. This process must be repeated for each mode of motion. The total potential for all 6 DOF is then [43].

$$\Phi = \sum_{j=1}^{6} \phi_j \dot{\alpha}_j \tag{3.12}$$

where Φ is the total velocity potential, ϕ_j the unit potential for the j^{th} mode of motion, and $\dot{\alpha}_j$ is the time derivative of the body motion for the j^{th} mode of motion. We next present the application of the Green's Theorem for nonlinear time-domain wave-body interaction problem which was originally developed by Longuet-Higgins and Cokelet [36] and commonly referred to as the mixed Eulerian-Lagrangian (MEL) formulation.

3.2.2 Non-Linear Time Domain Analysis for Wave-Body Interactions

In this section, we discuss the formulation of the boundary integral equation for the non-linear time domain. This procedure requires higher processor requirements compared to the frequency domain due to the necessary multi-step MEL process. In non-linear time domain, the sea surface and body boundaries are considered time dependent requiring boundary position updates after each time step. To update the position, we utilize the MEL scheme to first solve the unknown variables on the current boundary location and then use the boundary conditions to update their position. From Chapter 2, we revisit the non-linear free surface, body, far-field, and sea floor boundary conditions:

$$\left.\begin{aligned} &\frac{D\phi}{Dt} = \frac{1}{2}\left|\nabla\phi\right|^2 - gz \\ &\frac{Dx}{Dt} = \frac{\partial\phi}{\partial x} \\ &\frac{Dy}{Dt} = \frac{\partial\phi}{\partial y} \\ &\frac{Dz}{Dt} = \frac{\partial\phi}{\partial z} \end{aligned}\right\} \quad \text{on the free surface } (F)$$

$$\frac{\partial\phi}{\partial n} = \vec{V}\cdot\hat{n} + \vec{\Omega}\cdot\left(r\times\hat{n}\right) \qquad \text{on the body } (H)$$

$$\phi = 0 \qquad \text{on the far-field } \left(\Sigma\right)$$

$$\frac{\partial\phi}{\partial n} = 0 \qquad \text{on the sea floor } \left(B\right) \tag{3.13}$$

Utilizing these equations with initial conditions (calm free surface and stationary body), we formulate the wave-body interaction equation for the initial time step. This equation for the non-linear time domain is presented below:

$$\begin{aligned} &2\pi\phi(P) + \int_H \phi\frac{\partial}{\partial n}\frac{1}{r}dH - \int_F \frac{\partial\phi}{\partial n}\frac{1}{r}dF - \int_\Sigma \frac{\partial\phi}{\partial n}\frac{1}{r}d\Sigma - \int_B \frac{\partial\phi}{\partial n}\frac{1}{r}dB \\ &= \int_H \frac{1}{r}\frac{\partial\phi}{\partial n}dH - \int_F \phi\frac{\partial}{\partial n}\frac{1}{r}dF - \int_\Sigma \phi\frac{\partial}{\partial n}\frac{1}{r}d\Sigma \end{aligned} \tag{3.14}$$

Equation (3.14) is solved for the unknown variables on the left hand side for the initial time step. After solving this Eulerian step of the MEL scheme, the new boundary locations are updated using the conditions from equation (3.13). Following this update, the time is advanced using a small time step and the process is repeated until the desired elapsed time is reached.

In this chapter, we have presented the derivations involved in the boundary integral equations for the wave-body interaction problem presented as the main focus of this thesis. We first derived these equations for linearized frequency domain analysis and then for non-linear time domain analysis. In the following chapter, we discuss the derivation and relation of the wave forces acting on a floating or submerged body followed by the modeling of sea state spectra and determining the body response spectra.

CHAPTER 4: WAVE FORCES AND VEHICLE RESPONSE

To determine body response to waves, we begin Chapter 4 by defining the wave forces acting on a submerged or surface-piercing body, namely the radiating and exciting wave forces. Using these forces, the 6 DOF equations of motion are formulated followed by using these equations to solve for the response amplitude operator (R.A.O) of motion. Next we discuss the different techniques for modeling the sea state for various weather and geographical situations. Finally, we derived the body response spectra equation by combining the R.A.O. as a transfer function with the sea state model.

4.1 Wave Forces

Next a review on the response of a submerged body to wave forces is presented. The problem is illustrated in Figure 4-1.

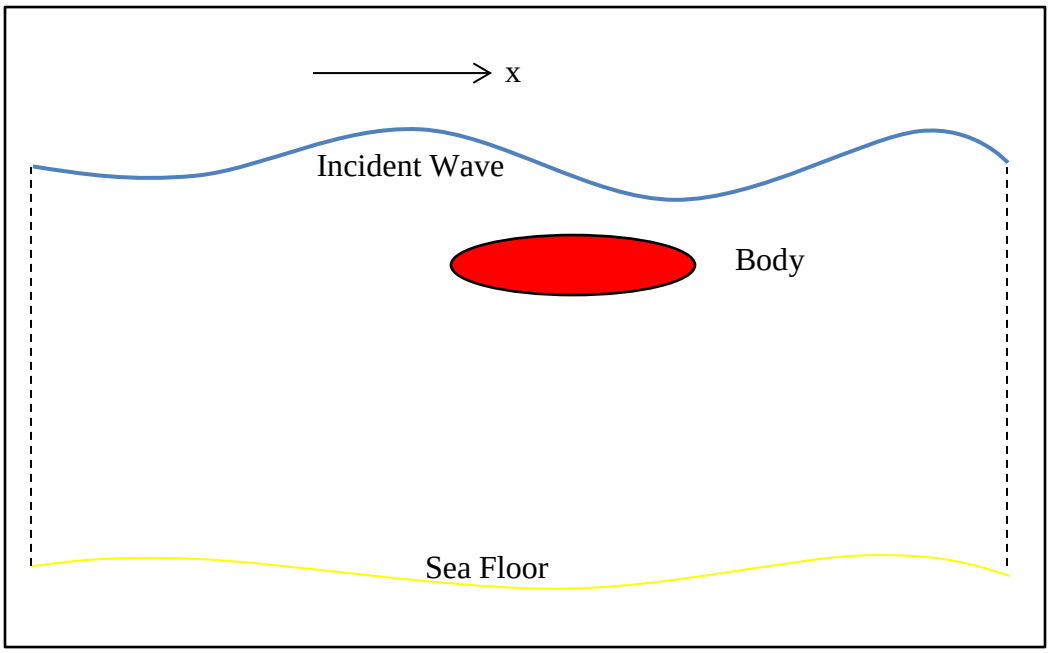

Figure 4-1: Submerged Body

In figure 4-1, the incident wave travels in the positive *x* direction and as the wave contacts the body, the wave diffracts around the body. This wave energy causes body oscillation and a portion of the energy is then transferred back to the fluid in the form of outwardly radiating waves [14]. These waves are studied as two separate forces, namely the wave radiating force and the wave exciting force. In the linear wave-body interaction problem, the wave exciting force consists of the incident and diffracted wave forces while the radiating force consists of the added mass and damping forces. These forces can be analyzed separately only in the linearized problem as attempted in this thesis and are discussed in the next section.

4.1.1 Wave Radiating Force and Wave Exciting Force

To begin, we break down the total wave force acting on a body as the sum of the incident wave force, diffracted wave force, and radiated wave force.

$$\mathbf{F} = F^I + F^D + F^R \tag{4.1}$$

As mentioned above, the radiation force is caused by the radiating waves traveling outward from the oscillating body. This force is made up of two components, the added mass component and the wave damping component with the added mass proportional to the body acceleration and the wave damping proportional to velocity. As shown in Yeung [63], for the body motion in the form:

$$\alpha_j = \mathrm{Re}\left(A_j e^{-i^* \sigma t}\right) \tag{4.2}$$

the unit radiation force can be written as:

$$f_{ij}^R = -\mu_{ij}\ddot{\alpha} - \lambda_{ij}\dot{\alpha} \tag{4.3}$$

where, f_{ij}^{R} is the force in the i^{th} direction due to motion in the j^{th} direction, μ_{ij} denotes the added mass coefficient and λ_{ij} the wave damping. In terms of the potential on the body surface, f_{ij}^{R} is given by:

$$f_{ij}^{R} = \int_{s} \rho \phi_j \hat{n}_j dS = \mu_{ij} + i^{*} \frac{1}{\sigma} \lambda_{ij} \tag{4.4}$$

For a body length much smaller than the incident wave length, the diffraction force is negligible and can be dropped from equation 4.1. The incident force stems from the incident pressure which can take the following form:

$$P^{I} = \rho g \frac{H}{2} \frac{\cosh\left(k\left(z+h\right)\right)}{\cosh\left(kh\right)} e^{i^{*}(kx-\sigma t)} \tag{4.5}$$

where H is the incident wave height, k the wave number, and h the water depth. The incident force is determined from the surface integral of the pressure.

$$F_{j}^{I} = \int_{S_0} \rho g \frac{H}{2} \frac{\cosh\left(k\left(z+h\right)\right)}{\cosh\left(kh\right)} e^{i^{*}(kx-\sigma t)} \cdot \hat{n}_j dS_0 \tag{4.6}$$

where F_{j}^{I} is the incident wave force in the j^{th} direction.

4.2 Transfer Function

To determine the body motion, we join together the incident and radiated wave forces in the following six linear equations of motion.

$$\sum_{i=1}^{6} \left[-\sigma^2 \left(m_{ij} + \mu_{ij} \right) + i\sigma\lambda_{ij} + c_{ij} \right] \xi_i = F_j^{I} \tag{4.7}$$

where m_{ij} is the body mass and inertia component which takes the following form:

$$m_{ij} = \begin{Bmatrix} m & 0 & 0 & 0 & -mz_g & 0 \\ 0 & m & 0 & mz_G & 0 & 0 \\ 0 & 0 & m & 0 & 0 & 0 \\ 0 & mz_G & 0 & I_{11} & I_{12} & I_{13} \\ -mz_G & 0 & 0 & I_{21} & I_{22} & I_{23} \\ 0 & 0 & 0 & I_{31} & I_{32} & I_{33} \end{Bmatrix} \tag{4.8}$$

In equation (4.8), the horizontal row represents the *i* coefficients from 1 to 6 while the vertical row represents the *j* coefficients from 1 to 6, *m* is the mass of the body, $\left(x_g, y_g, z_g\right)$ the coordinates for the center of gravity of the body and I_{ij} is the moment of inertia. In equation (4.7), the c_{ij} term has the following form:

$$\begin{aligned} c_{44} &= \rho g \forall \left(z_B - z_G\right) \\ c_{55} &= \rho g \forall \left(z_B - z_G\right) \\ c_{46} &= -g\left(\rho \forall x_B - m x_G\right) \\ c_{56} &= -g\left(\rho \forall y_B - m y_G\right) \end{aligned} \tag{4.9}$$

where $\forall$ the submerged volume, and $\left(x_B, y_B, z_B\right)$ the coordinates for the center of buoyancy. All other values of *(i,j)*, $c_{ij} = 0$.

For incident waves of unit wave amplitude: $\frac{H}{2} = 1$, the amplitude of the transfer function is called the response amplitude operator (R.A.O.). Substituting and manipulation of equation (4.7) solves for the body transfer function for the i^{th} mode of motion [43]:

$$\xi_i = \sum_{j=1}^{6} \left[-\sigma^2 \left(m_{ij} + \mu_{ij}\right) - i\sigma\lambda_{ij} + c_{ij} \right]^{-1} F_j^I \tag{4.10}$$

Note that the result from equation (4.10) only corresponds to a single angular frequency value. Next, we present the method used to model the sea spectra for a given sea state.

4.3 Modeling Sea State

Formulations for numerically modeling ocean conditions have been used for decades. These important formulations are used to predict how the sea surface will act with certain weather and geographical conditions and many different techniques are available. One of the original sea spectra models developed was the Pierson-Moskowitz spectrum. This spectrum was created in 1964 and defines the empirical relation between the distribution of wave energy and frequency [43]. This model was derived using observations taken from the North Sea and is ideally designed for areas with fully developed seas located large distances from shore. However, many times data is sought for areas where this is not the case. The JONSWAP method was derived from the Pierson-Moskowitz spectrum and is used for predicting sea states close to shore where seas may not be fully developed [22]. This spectrum allows waves to grow as a function of wind speed and distance from shore. However, the JONSWAP method does not allow for shallow water depth and therefore cannot accurately model the sea state in areas commonly described as ‘near shore’ where waves are entering shallower water from deeper waters. To better model these near shore areas, the TMA Sea Spectra formulation was derived from both the Pierson-Moskowitz and JONSWAP methods [22]. The acronym TMA represents the first letter from the three testing sites used to validate the formulation. The letters stand for Texel (testing location at the Texel lightship west of Rotterdam in the southern North Sea), MARSEN (Marine Remote Sensing Experiment at the North Sea) and ARSLOE (Atlantic Remote Sensing Land Ocean Experiment) [22]. The TMA spectrum contains many input variables which allow for a higher level of customization of the sea spectrum. This spectrum was formulated by Hughes in 1984

and includes a ‘limited depth’ variable from his realization that long-period waves must have a limited height in the shallow waters commonly found near shore [22]. Due to this complexity of the TWA spectra equation and many variables, the details and description of the formulas can be found in Appendix B. Next, we complete the problem by combining the TWA sea state model with the body transfer function and obtain the total body response spectrum.

4.4 Body Response Spectrum

The transfer function from equation (4.5) is combined with the TMA sea state spectrum in the following from.

$$S_{\xi\xi} = |\xi|^2 \cdot S_{xx} \tag{4.11}$$

where $S_{\xi\xi}$ is the response spectrum of the body and S_{xx} is the sea state spectrum $S(\omega)$ for a wave traveling in the positive x-direction [43]. These results are plotted against the frequency spectrum to show the amplitude of the body response over a range of frequencies in varying sea state conditions. This tool is utilized to predict vehicle response without the expensive development of prototypes and testing. Now that the formulation of the response spectrum is obtained, we move on to Chapter 5 where the numerical procedures of the algorithm are defined and explained.

CHAPTER 5: NUMERICAL PROCEDURES

In this chapter, we focus on the algorithmic procedures used to solve this thesis problem by first explaining the techniques used to discretize the body and fluid boundaries from continuous models into discrete models followed by the presentation and explanation of the matrix equations and how to solve them. At the end of the chapter, we discuss the particular application of the above techniques to the linear frequency domain.

5.1 Boundary Discretizations

To simplify the mathematical computations, we discretize the body and fluid boundaries into small panels. One must be cautious in the method used to discretize each boundary as the size of the panel and its location on the surface affects the accuracy of the result. In the following sections, each boundary and the method used to discretize the surface is discussed and shown.

5.1.1 Discretization of the Body

We begin with discretizing the body surface. As an example, consider a prolate spheroid with major axis radius a along the x-axis and minor axis radius b along the y and z axis. By discretizing the surface into small panels, we assume that the velocity potential remains constant over the entire panel. The panels should be significantly small especially in areas where a drastic geometric shape change occurs (i.e. at the poles). In figure 5-1, an example of a discretized prolate spheroid is shown. It is seen that the panels

near the poles of the spheroid are smaller compared to those panels around the mid-body. The pole areas contain more drastic changes in geometric shape and have a larger flow gradient requiring smaller panels to obtain constant potential throughout the panel.

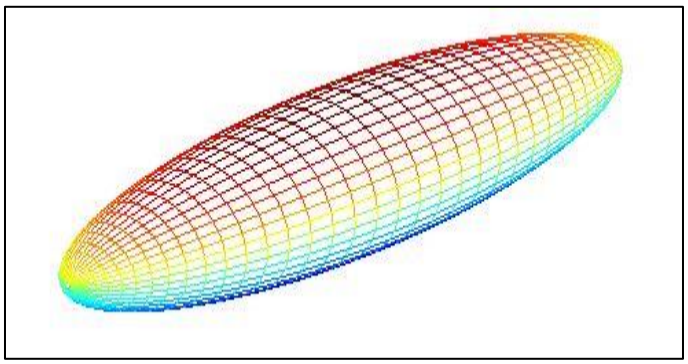

Figure 5-1**:** Discretized body

We next begin to discretize the fluid boundaries that surround the body. In the next section we describe the different techniques that can be used to discretize the circular sea surface and sea floor.

5.1.2 Discretization of the Sea Surface and the Sea Floor

The sea surface, sea floor and far-field boundary when combined will form a cylindrical fluid domain. To begin we start with the circular sea surface and sea floor. When discretizing these boundaries, one must express due caution as there are many possible discretization methods and each affect the accuracy of the solution. We start by discretizing the sea surface using the spider mesh method. This type of circular meshing creates a ‘pie shape’ panel with a constant number of slices around the entire surface as shown in figure 5-2 below.

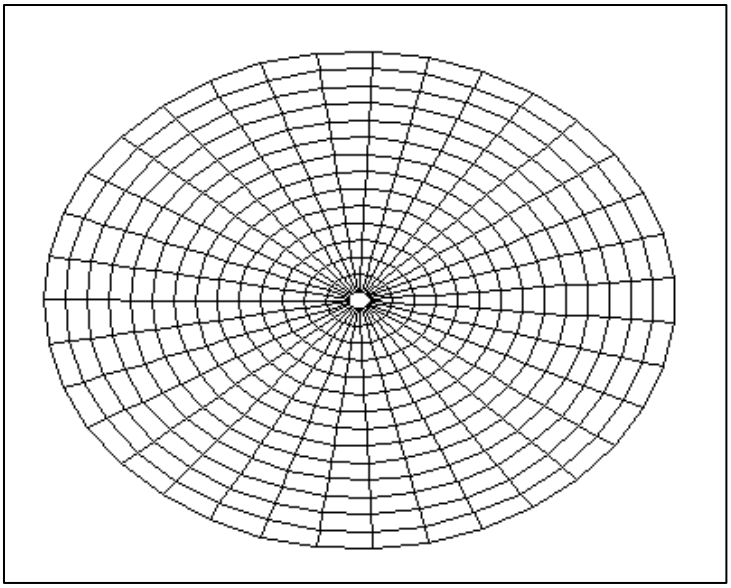

Figure 5-2: Spider Meshing

Note that as the distance from the center increases, the panel size becomes larger which can lead to error. In order to mitigate this, the number of slices must be increased which then leads to singularities at the center. To solve this issue, we utilize a different circular meshing technique where the number of slices increases as the distance from the center increases. This meshing technique is shown in figure 5-3 below.

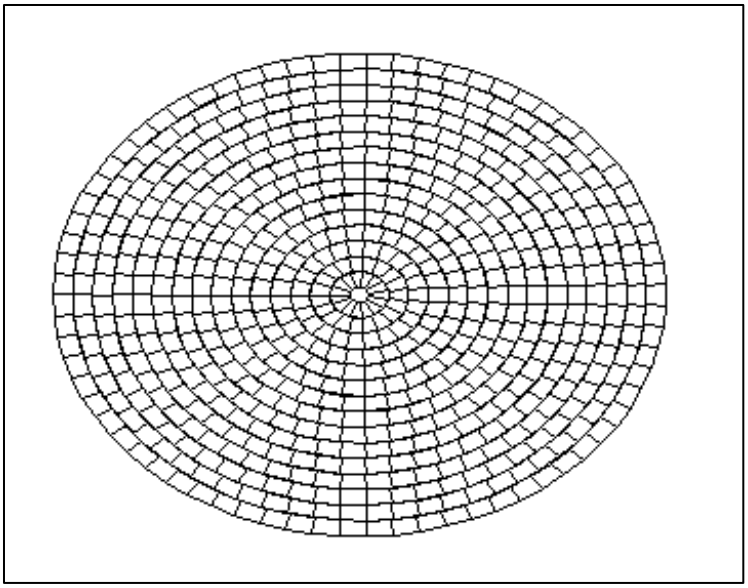

Figure 5-3: Circular Meshing

Note with this technique that all panels have a similar area and no singularities are created. Using this circular meshing technique decreases error and increases accuracy.

Since the sea floor and sea surface have the same shape, the sea floor is discretized in the same manner as the sea surface but separated by the water depth distance. To complete the fluid domain, we next discretize the far-field boundary followed by a 3-D rendering of the fluid domain in entirety.

5.1.3 Discretization of the Far-Field Boundary

We continue with the cylindrical fluid domain shape and model the far-field boundary in the shape of an open ended cylinder. Similar to the previous surfaces, the panel size must be small enough in order to assume constant velocity potential over the panel. The panel size remains constant throughout the water column, small enough to maintain accuracy but large enough to avoid singularities and maintain computational efficiency. Figure 5-4 below shows the cylindrical fluid domain in its discretized state.

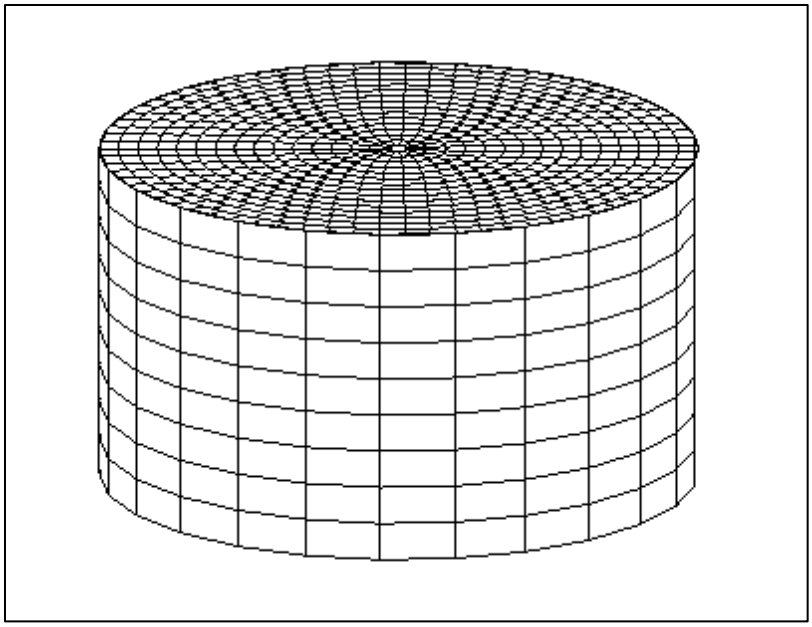

Figure 5-4: Discretized Fluid Domain

In the next section, we present the procedures to solve the wave-body interaction problem by using the recently discretized boundaries.

5.2 Influence Coefficients

In order to solve the analytical form of Green's integral (equation 3.7), the equation is converted into matrix equation form and solved numerically. The matrix equation form takes the following form:

$$\begin{bmatrix} A_{PQ} & A_{PQ} & A_{PQ} \\ A_{PQ} & A_{PQ} & A_{PQ} \\ A_{PQ} & A_{PQ} & A_{PQ} \end{bmatrix} \cdot \begin{Bmatrix} x_P \\ x_P \\ x_P \end{Bmatrix} = \begin{bmatrix} b_Q \\ b_Q \\ b_Q \end{bmatrix} \tag{5.1}$$

where P and Q represent the field panel and source panel number respectively, *A* represents the influence coefficient, *x* the unknown variable, and *b* the known value from the left hand side.

5.2.1 Solving for Linear Frequency Domain Coefficients

In the linear frequency domain, equation (3.11) was presented with the unknowns on the left hand side of the equation and the known quantities on the right hand side of the equation. The boundary integral equation is written in index notation form as $A_{PQ}\phi_P = b_Q$ with the unknown velocity potential represented as ϕ_P and *P* and *Q* as the field point and source point respectively. The influence coefficient A_{PQ} is a square matrix holding the coefficients for the velocity potential and b_Q is the column vector filled with the known values from the right hand side of the equation. Next, the original boundary integral equation is presented in equation (5.2), followed by its equivalent matrix form in equation (5.3).

$$2\pi\phi_j(P) + \int_H \phi_j \frac{\partial}{\partial n}\frac{1}{r} dH + \int_B \phi_j \frac{\partial}{\partial n}\frac{1}{r} dB + \int_F \phi_j \left[\frac{\partial}{\partial n}\frac{1}{r} - \frac{\sigma^2}{g}\frac{1}{r}\right] dF + \int_\Sigma \phi_j \left[\frac{\partial}{\partial n}\frac{1}{r} - \left(-\frac{1}{2R} + ik\right)\frac{1}{r}\right] d\Sigma = \int_H \frac{\hat{n}_j}{r} dH \tag{5.2}$$

$$\begin{bmatrix} A_{HH} & A_{HB} & A_{HF} & A_{H\Sigma} \\ A_{BH} & A_{BB} & A_{BF} & A_{B\Sigma} \\ A_{FH} & A_{FB} & A_{FF} & A_{F\Sigma} \\ A_{\Sigma H} & A_{\Sigma B} & A_{\Sigma F} & A_{\Sigma\Sigma} \end{bmatrix} \cdot \begin{Bmatrix} \phi_H \\ \phi_B \\ \phi_F \\ \phi_\Sigma \end{Bmatrix} = \begin{bmatrix} b_{HH} \\ b_{BH} \\ b_{FH} \\ b_{\Sigma H} \end{bmatrix} \tag{5.3}$$

In equation (5.3), the first subscript for coefficient *A* and *b* represents the boundary on which the field point resides and the second subscript represents the boundary on which the source point resides. After filling the cells within *A* and *b* using

the coefficients from equation (5.2), the system is solved numerically for the unknown variable ϕ_P by completing LU decomposition. By inverting matrix *A* and multiplying by *b*, the unknown variables are determined for each panel as seen in the following equation [40]:

$$\phi_P = A_{PQ}^{-1} \cdot b_Q \tag{5.4}$$

Equation (5.4) solves for the unit potential on each panel *P* for the j^{th} mode of body motion. After solving each unit potential, the total potential is determined by the use of equation (5.5).

$$\Phi = \sum_{j=1}^{6} \phi_j \dot{\alpha}_j \tag{5.5}$$

This represents the total potential for the selected frequency value. Next, we describe the procedure to solve the boundary integral equation in the non-linear time domain.

5.2.2 Solving for Non-Linear Time Domain Coefficients

In the non-linear time domain analysis we use equation (3.11) to solve for the unknown variables in the same manner presented in section 5.2.1. The equation is presented here:

$$\begin{aligned} &2\pi\phi(P) + \int_H \phi \frac{\partial}{\partial n}\frac{1}{r} dH - \int_F \frac{\partial \phi}{\partial n}\frac{1}{r} dF - \int_\Sigma \frac{\partial \phi}{\partial n}\frac{1}{r} d\Sigma \\ &= \int_H \frac{1}{r}\frac{\partial \phi}{\partial n} dH - \int_F \phi \frac{\partial}{\partial n}\frac{1}{r} dF - \int_\Sigma \phi \frac{\partial}{\partial n}\frac{1}{r} d\Sigma \end{aligned} \tag{5.6}$$

Due to the time dependent boundaries, solving equation (5.6) is more complex than the linear frequency domain equation (5.2). As previously mentioned, the boundaries are dynamic in the time domain and their new location must be calculated for each time step.

Since the entire matrix equation for both *A* and *b* must be updated for each step, LU decomposition is very time and processor intensive. To mitigate this issue, iterative solvers take the place of numerically solving the problem. These techniques are explained in Appendix C.

5.3 Free Surface Advancement for Time Domain Analysis

In time domain analysis, the boundary conditions are used to advance the free-surface position over time. Once the surface is updated, the boundary integral equation is solved for the next time step and the procedure is repeated. In this section, the techniques used to advance the free surface are presented.

Derived in Chapter 2, the dynamic and kinematic free surface boundary conditions in Lagrangian form are as follows:

$$\frac{D\phi}{Dt} = \frac{1}{2}\left|\nabla\phi\right|^2 - gz \quad \text{dynamic free surface condition}$$

$$\left.\begin{aligned} \frac{Dx}{Dt} &= \frac{\partial\phi}{\partial x} \\ \frac{Dy}{Dt} &= \frac{\partial\phi}{\partial y} \\ \frac{Dz}{Dt} &= \frac{\partial\phi}{\partial z} \end{aligned}\right\} \quad \text{kinematic free surface condition}$$

Here, the forward Euler method is used to determine the velocity potential and surface particle location for the next time step. Below, the free surface conditions are transformed using numerical time-integration techniques.

$$
\begin{aligned}
&\frac{D\phi}{Dt} = \frac{1}{2}\left|\nabla\phi\right|^2 - gz \;\rightarrow\; \phi^{t+1} = \phi^t + \Delta t\left(\frac{1}{2}\left|\nabla\phi^t\right|^2 - g\eta^t\right)\\
&\frac{Dx}{Dt} = \frac{\partial\phi}{\partial x} \qquad\qquad \rightarrow x^{t+1} = x^t + \Delta t\left(\frac{\partial\phi}{\partial x}\right)\\
&\frac{Dy}{Dt} = \frac{\partial\phi}{\partial y} \qquad\qquad \rightarrow y^{t+1} = y^t + \Delta t\left(\frac{\partial\phi}{\partial y}\right)\\
&\frac{Dz}{Dt} = \frac{\partial\phi}{\partial z} \qquad\qquad \rightarrow \mathrm{z}^{t+1} = z^t + \Delta t\left(\frac{\partial\phi}{\partial x}\right)
\end{aligned}
\tag{5.7}
$$

Solving equation (5.7) yields the velocity potential on the free surface as well as the (*x*,*y*,*z)* position of a surface particle for the next time step. Research has shown that equation (5.7) can create numerical instabilities. To mitigate this issue, higher order numerical schemes should be used. Two widely used higher order schemes are the 4th Order Adams-Bashforth-Moulton scheme and the 4th Order Runge-Kutta scheme. The details for these schemes can be found in Appendix C.

5.4 Algorithmic Procedures

An algorithm was created to solve the linearized frequency domain wave-body interaction problem. In this section, the algorithmic procedures are explained in detail.

5.4.1 Linear Frequency Domain

The following steps represent the procedures required to solve the problem in the linearized frequency domain:

1. Choose angular frequency value
2. Create and discretize all surfaces present within the fluid domain
3. Calculate area, normal vector (pointing out of fluid as per Green's Theorem), and coordinates of the midpoint of each panel on the boundary surfaces

4. Calculate the coefficients for square matrix *A* and column vector *b*
5. Using LU-decomposition, solve for the unknown quantity for each panel
6. Solve for hydrodynamic coefficients
7. Solve steps 1-6 for remaining angular frequency values
8. Combine the hydrodynamic coefficients with the incident wave to determine the transfer function
9. Utilize TMA sea spectra formulations to model sea state spectra for particular environmental settings
10. Combine TMA sea spectra with transfer function to determine total body response spectra

CHAPTER 6: RESULTS AND DISCUSSION

The results obtained using the boundary-integral methods for the added mass and damping are presented in this chapter along with a comparative study involving simple geometries for validation of the numerical model.

6.1 Algorithm Validation

Before analyzing various submerged body shapes for hydrodynamic coefficients and response characteristics in waves, we first validate the algorithm created for this project. In order to do this, we revisit a paper written by Wu and Taylor [54], where they studied the radiation of spheroids of various aspect ratios. In their results, they present detailed findings for a prolate spheroid with an aspect ratio of 6/1. The major axis was in the horizontal direction and had a length of *1 [m]* with the minor axis along the remaining two axis set to *1/6 [m]*. Measured from the sea surface to the horizontal axis of the body, the submergence depth was set as *h =1/3 [m]*. Using these values for vehicle dimensions the added mass and wave damping results from the created algorithm were compared to those presented by Wu and Taylor. In Wu and Taylor's paper, the results are normalized by the mass of the fluid displaced by the body. The added mass and wave damping coefficients are normalized by $\frac{4}{3}\pi\rho ab^2$, where a is the major axis radius and b is the minor axis radius. This leaves the added mass coefficient dimensionless but the wave damping will have a dimension of frequency. In order to compare solutions one-to-one,

we normalize our results in the same manner. The comparison between Wu and Taylor's results and the algorithm's results are presented in figures 6-1 and 6-2.

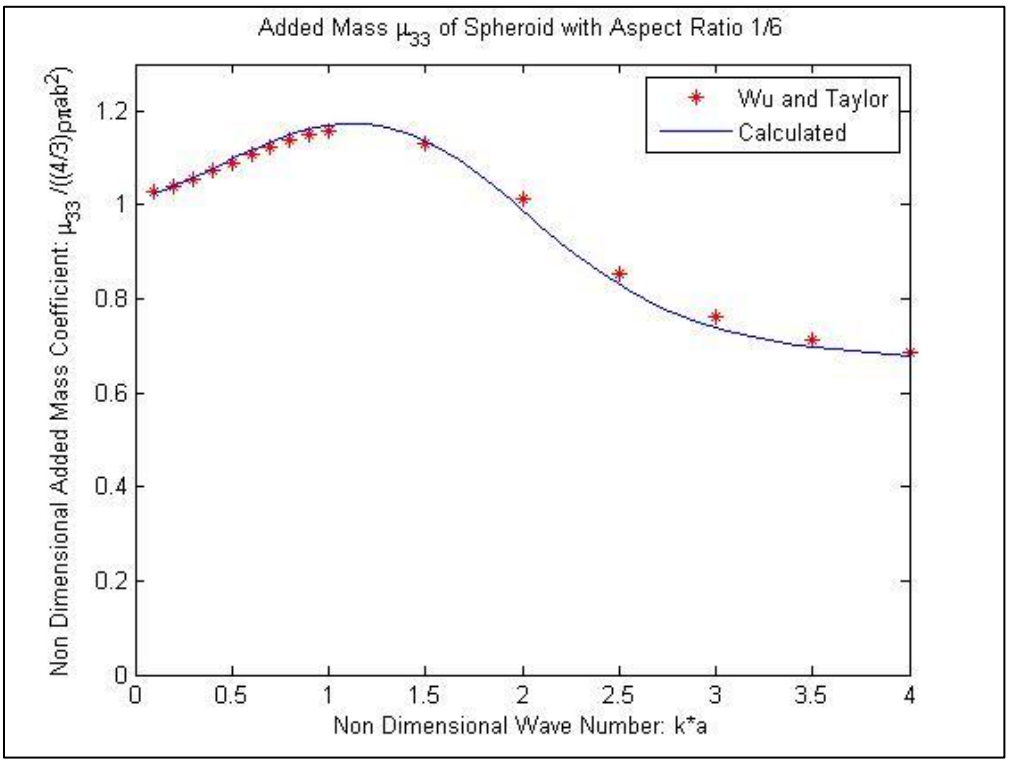

Figure 6-1: Added mass of submerged spheroid: Heave

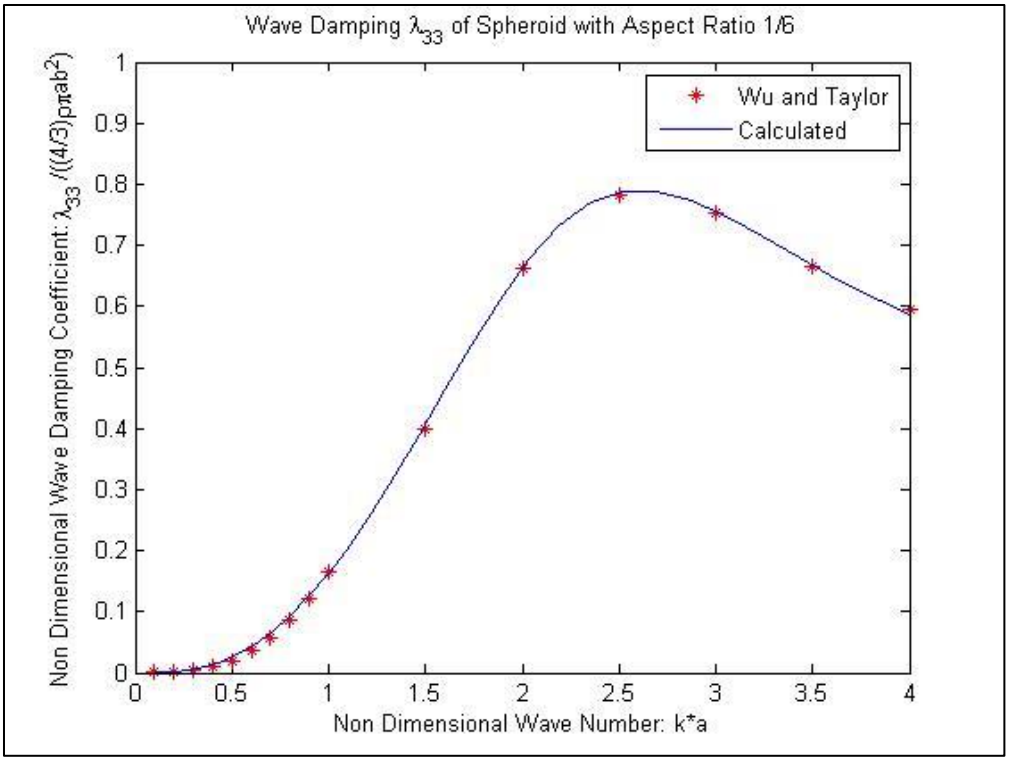

Figure 6-2: Wave damping for submerged spheroid: Heave

In figures 6-1 and 6-2 above, the blue line represents the calculated results from the algorithm developed for this project which is based on the frequency-domain boundary integral method, while the red stars represent the data presented in Wu and Taylor's paper. For the present method, 7610 panels were used with 1600 on the body, 3690 on the free surface, 1600 on the far field, and 720 on the sea floor. As can be observed, the results match quite well which thus validates the computer model developed for this research.

With the algorithm formulated correctly, we now analyze two families of body shapes using the theory and equations we have developed throughout this thesis. For simplicity we refer to the first hull shape as "Hull 1" and the second hull shape as "Hull 2". In order to compare the two hulls a typical vehicle volume and vehicle mass was

chosen based on a standard underwater vehicle. It is important to note that in order to keep the volume constant as the aspect ratio changed the overall length of the vehicle is also changed accordingly. One must use caution when comparing vehicles of different aspect ratios since the overall vehicle size differs, for example in pitch motion the vehicle response highly depends on the length of the body.

In this thesis, we focus on the three degrees of freedom namely heave, surge and pitch. These three degrees of freedom will allow adequate analysis of body shape in order to draw conclusions on the geometric factors that affect body response in waves. An extensive set of simulations were carried out for a large range of parameters and selected and representative results are only presented in this thesis for Hull1 and 2 as follows.

6.2 Hull 1: Spheroidal Parent Hull Form

The first hull form (Hull 1) studied is of a spheroidal shape. To make a rational and meaningful comparison of body geometry on radiation hydrodynamics, the ratio between the major and minor axis is changed while maintaining a constant volume. The results from the different ratios are analyzed to determine how shape affects the response of the vehicle. Figure 6-3 shows a rendering of the discretized spheroidal body for one chosen aspect ratio.

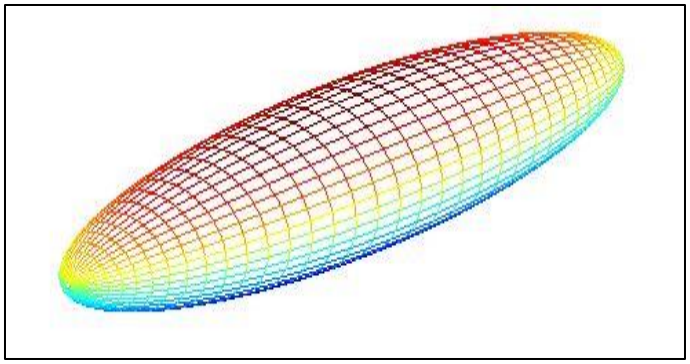

Figure 6-3: Spheroidal body shape of aspect ratio 6/1

6.2.1 Radiation Hydrodynamic Coefficients of Hull 1

In this section, we present the results for Hull 1 for various aspect ratios. Since we are focused on body shape, the depth of vehicle submergence and the water depth for each aspect ratio are kept constant at 1 [m] and 10 [m] respectively. In table 6-1 below, we present the geometric values of each body aspect ratio studied for the Hull 1 shape. Note that in table 6-1, the total body length and maximum diameter are presented but when normalizing the results, the radii values are used. The results are normalized by the mass of the fluid displaced by the body for the surge and heave motions $\left(0.25\rho\right)$ and by $\left(0.25\rho a^2\right)$ for pitch motion.

Aspect Ratio:	Total Length:	Diameter at Center:	Water Depth:	Submergence:
6/1	*2a = 2.58 [m]*	*2b = 0.43 [m]*	*10 [m]*	*1 [m]*
3/1	*2a = 1.626 [m]*	*2b = 0.542 [m]*	*10 [m]*	*1 [m]*
1/1	*2a = 0.78 [m]*	*2b = 0.78 [m]*	*10 [m]*	*1 [m]*

Table 6-1: Parameters of Hull 1 for displaced volume = 0.25 [m^3]

In figures 6-4 to 6-9, we present the radiation coefficients for Hull 1 for three degrees of freedom; surge, heave and pitch. The reader must keep in mind that although

all three body shapes for Hull 1 maintain a constant volume of 0.25 [m^3], the overall vehicle length is greater for an aspect ratio of 6/1 when compared to that of a sphere, as seen in table 6-1. The *y*-axis of each plot is labeled with the parameters used to normalize the results.

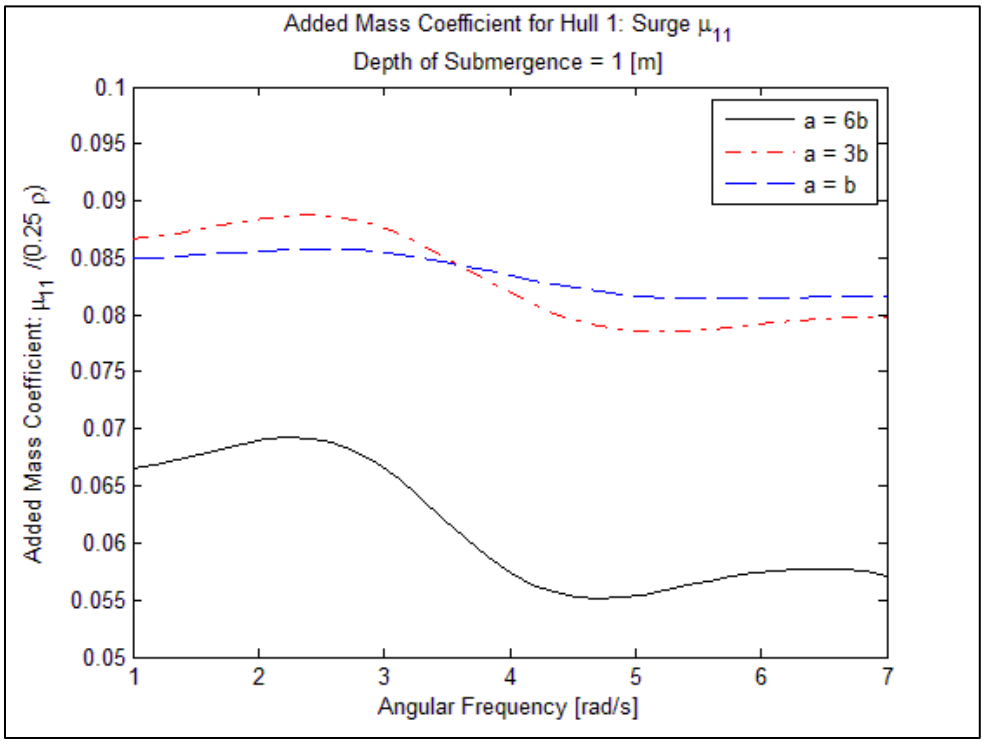

Figure 6-4: Added Mass for Hull 1: Surge

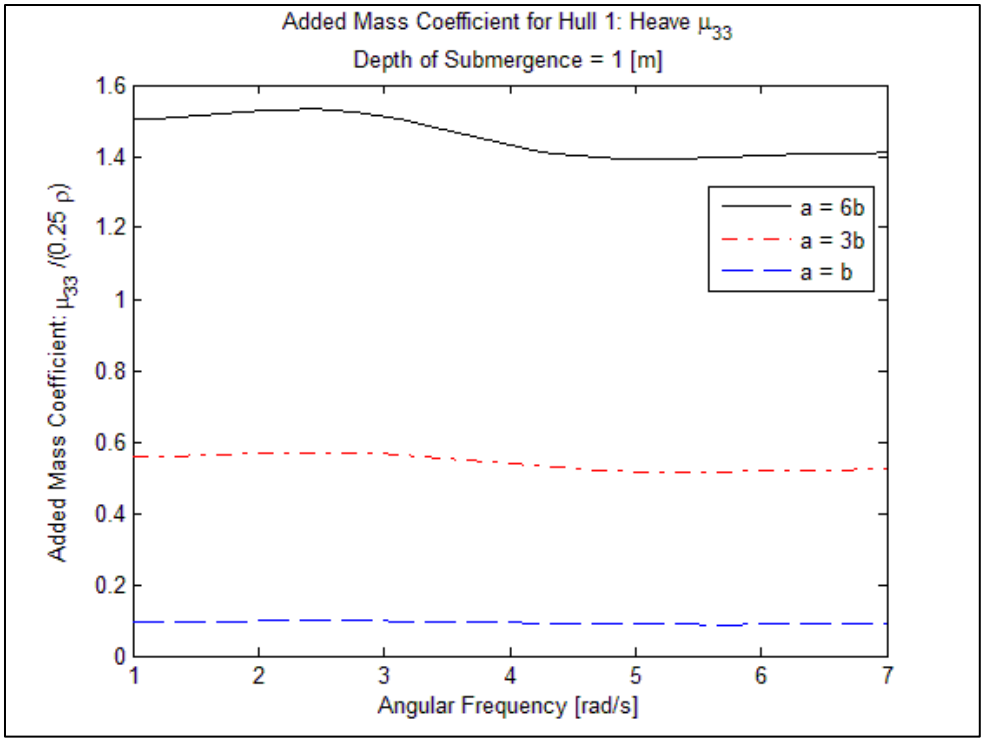

Figure 6-5: Added Mass for Hull 1: Heave

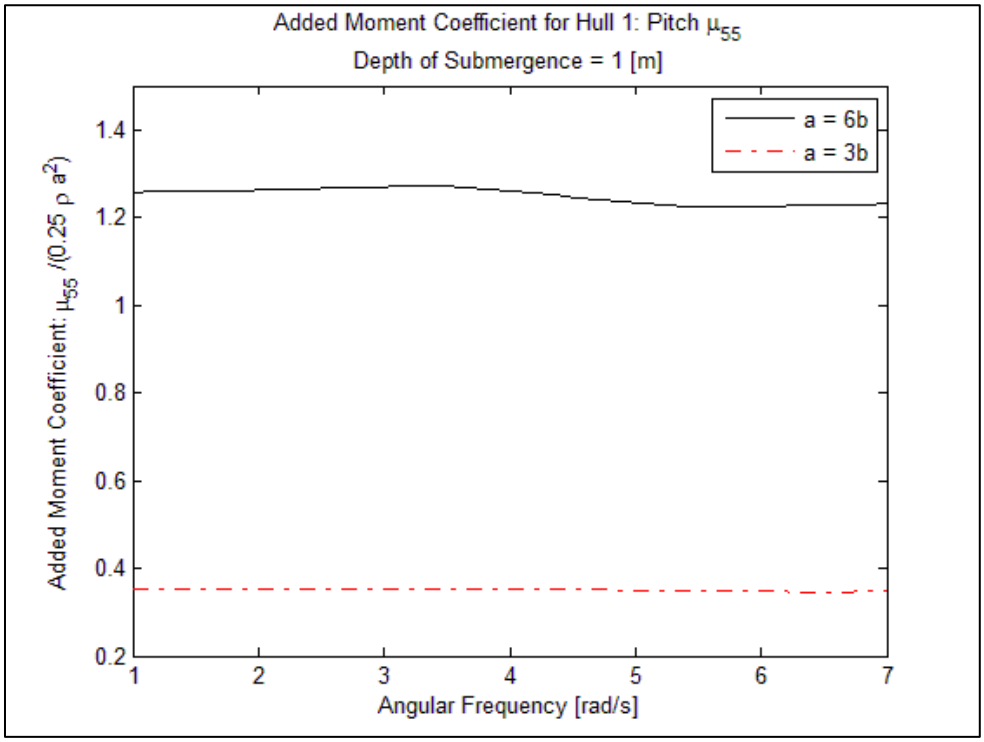

Figure 6-6: Added Moment of Inertia for Hull 1: Pitch

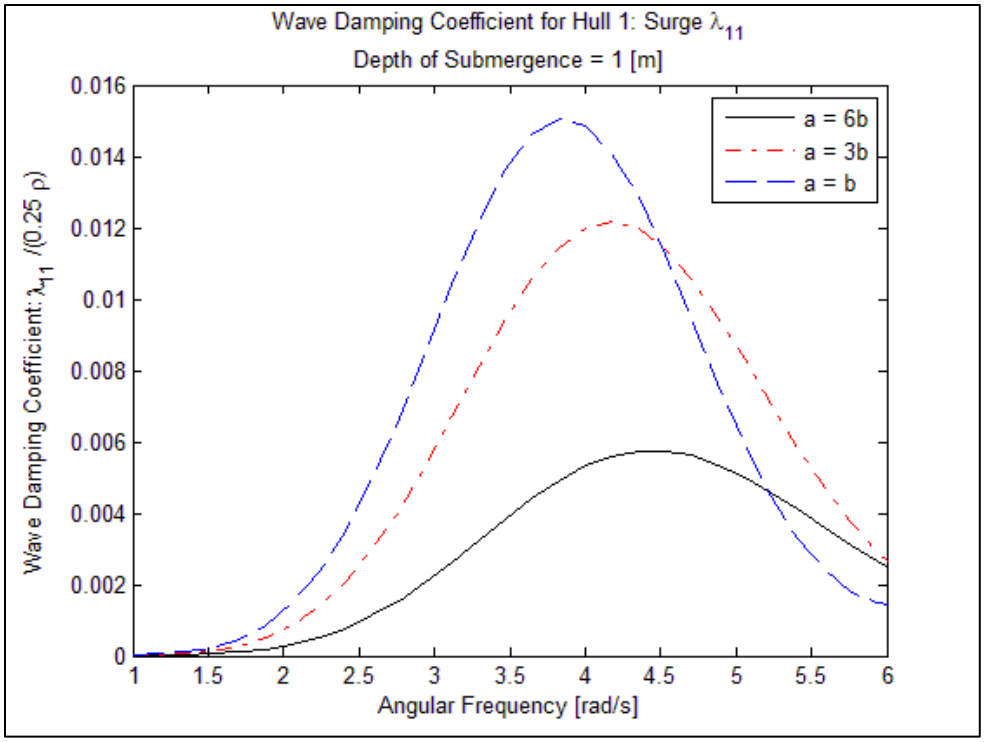

Figure 6-7: Wave Damping for Hull 1: Surge

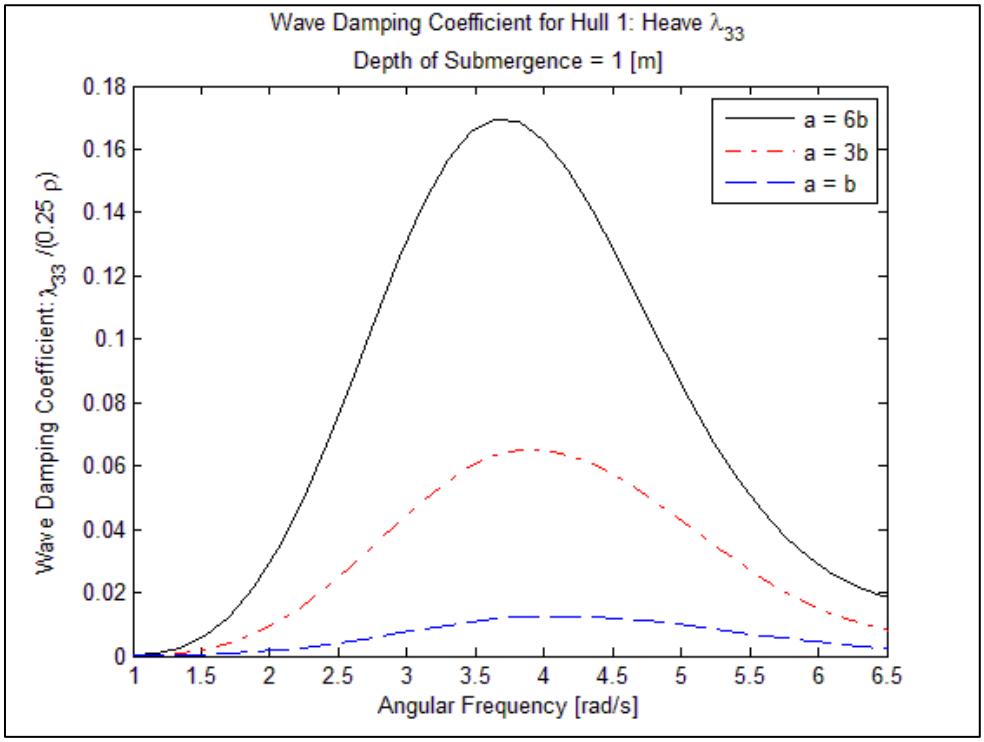

Figure 6-8: Wave Damping for Hull 1: Heave

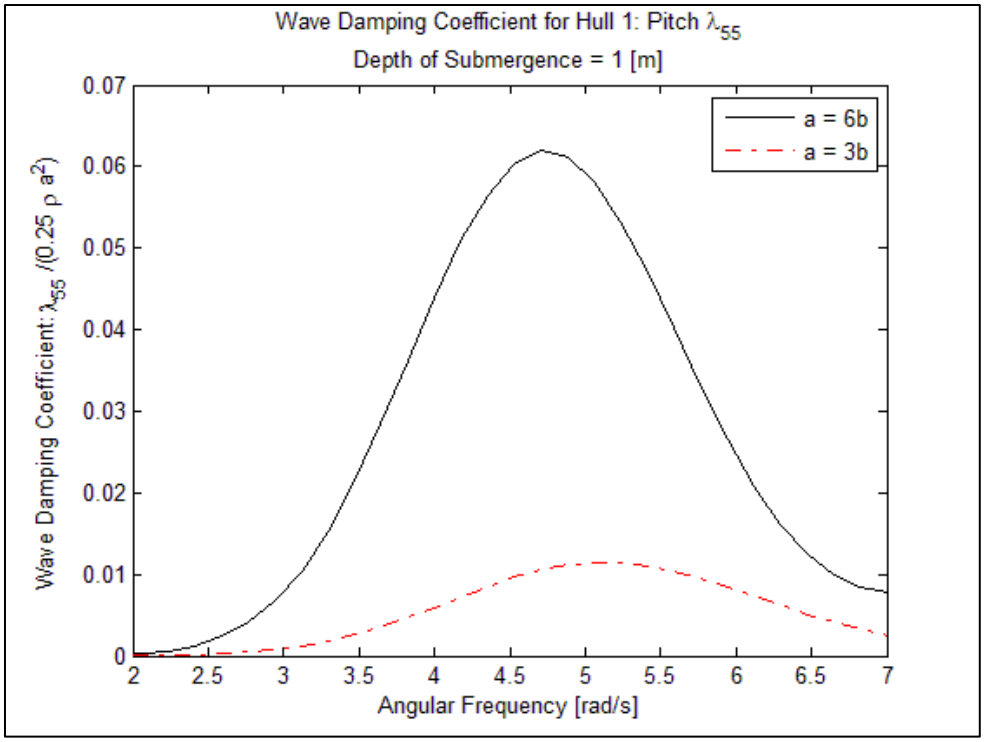

Figure 6-9: Wave Damping for Hull 1: Pitch

In figures 6-4 to 6-6, the added mass and added moment of inertia coefficients are presented for Hull 1. Figure 6-4 shows that a more slender body reduces the added mass in the surge direction. The surface area exposed in the *y-z* plane directly affects the added mass value and in the surge direction the body with aspect ratio $a = b$ has the greatest surface area in the *y-z* plane and therefore has greater added mass values. In figure 6-5, the added mass coefficient for heave motion increases for bodies with longer overall length. For heave motion, the body with the greatest length has the greatest surface area in the *x-y* plane causing higher added mass values. Figure 6-6 shows the added moment of inertia coefficients in the pitch direction. Here, the sphere ($a = b$) aspect ratio is omitted because hydrodynamic pitch moment for a sphere is zero in inviscid fluid. Additionally, it is seen that a longer body length ($a = 6b$) creates a larger moment arm associated with the pitch motion.

In figures 6-7 to 6-9, the wave damping coefficients are presented for each aspect ratio. For surge motion, figure 6-7, the sphere creates the largest wave damping values again due to the larger surface area in the *y*-*z* plane. Figure 6-8 shows the longer body creating higher wave damping values for heave motion, consistent with the previous results as the longer body has greater surface area in the *x*-*y* plane. Finally, figure 6-9 shows the relationship between the pitch wave damping and oscillation frequency. As before, the sphere aspect ratio was omitted as its rotation cannot generate waves in inviscid fluid. The results for pitch motion, figures 6-6 and 6-9, show larger coefficient values for the aspect ratio of 6/1, the longest body length, and have the largest distance between body tip and center of rotation. The longest body creates the largest moments for both inertia and damping force.

6.2.2. Hull 1 Transfer Function in Frequency Domain

With wave-exciting force taken to be Froude-Krylov force and the radiation forces as determined above using the boundary-integral method, we now determine the response transfer functions of Hull 1.

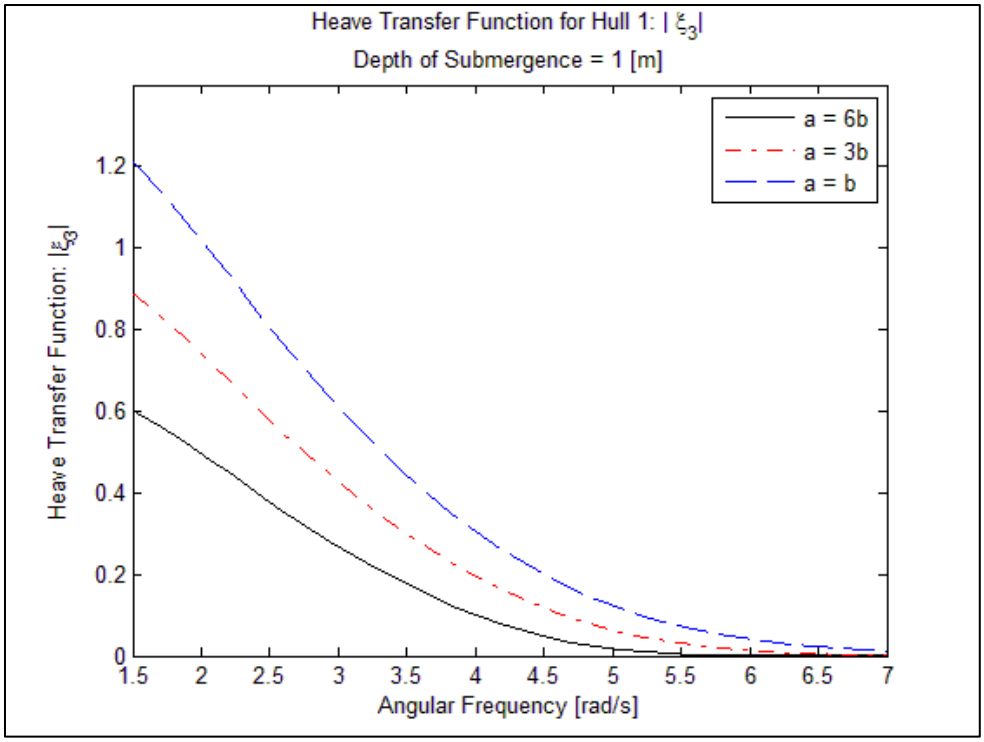

Figure 6-10: Heave Transfer Function for Hull 1

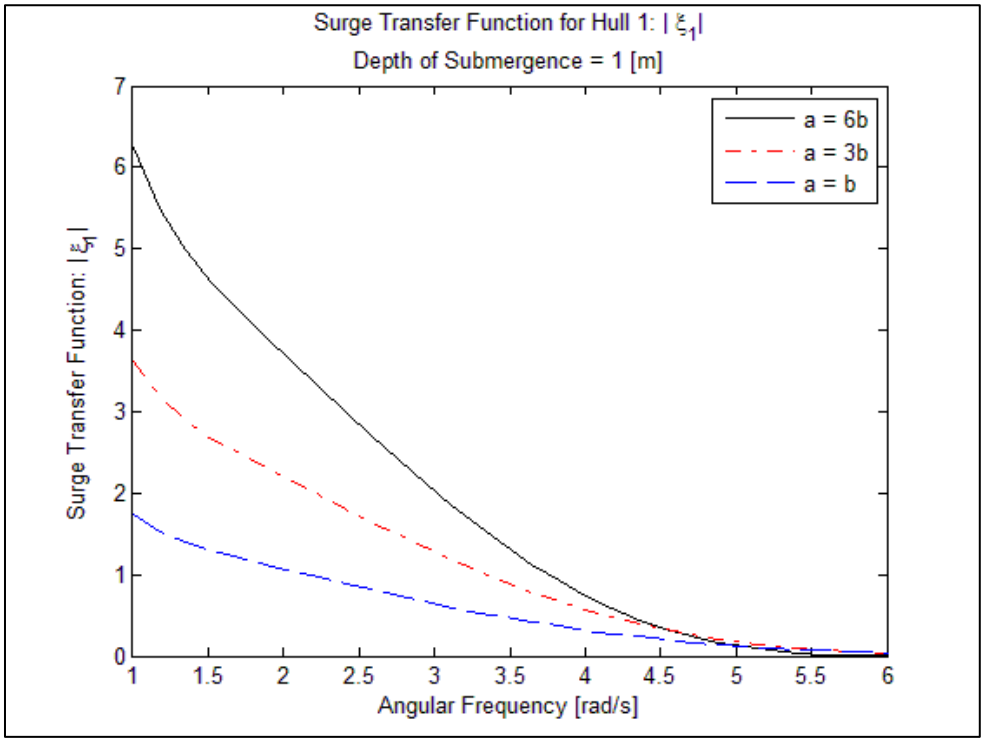

Figure 6-11: Surge Transfer Function for Hull 1

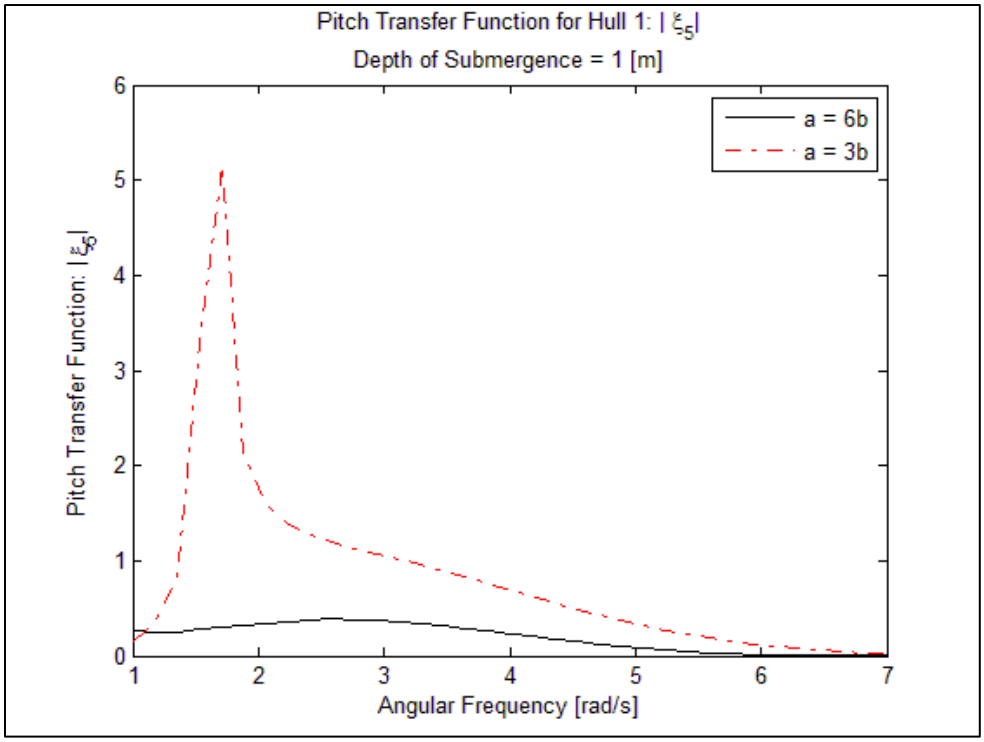

Figure 6-12: Pitch Transfer Function for Hull 1

In studying figures 6-10 to 6-12, it should be noted that the buoyancy restoring for heave and surge motions are zero, since the hull is submerged and the fluid is homogenous. There is however restoring pitch moment because of the positive metacentric height (GM= CG= 0.1*a*). Therefore the heave and surge response peaks at a wave number of zero. Without a restoring force, the response calculation becomes only a factor of the wave number and as wave number decreases, the response increases. In pitch motion of spheroid with *a = 3b*, the resonance frequency value is easily seen around the wave number of 0.25 [1/m]; here the metacentric height is set to be 0.163 [m].

6.3 Hull 2: Parallel Mid-Body

The second hull (Hull 2) studied utilizes a parallel mid-body section with a conical tail and shallow spheroidal nose. Figure 6-13 shows an example of the body shape.

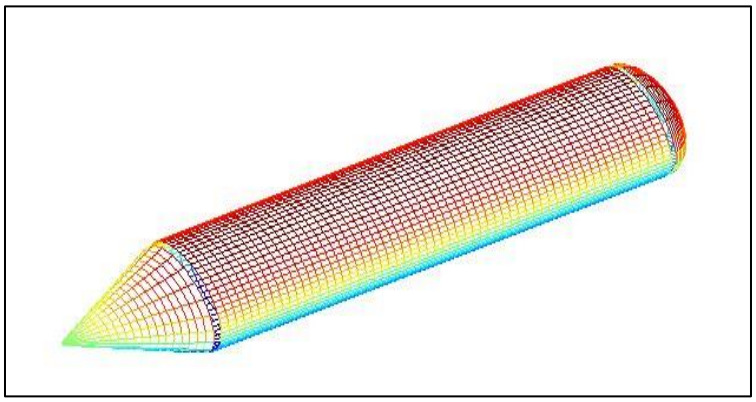

Figure 6-13: Parallel mid-body hull with aspect ratio 6/1

As mentioned earlier, the total body volume was kept constant and the same as Hull 1. When studying variations of Hull 2, the aspect ratio was determined as the ratio of the total length of the body to the diameter of the cylindrical mid-body. The length of the conical tail of Hull 2 represents 20% of the total vehicle length while the spheroidal nose represents 5% of the total vehicle length. These percentages and the three aspect ratios were chosen based on similar body shapes in use today [50]. Table 6-2 below displays a summary of the vehicle geometry of Hull 2. Note that in Table 6-2, the total body length and maximum diameter are presented as *2a* and *2b* respectively. To remain consistent with Hull 1, the results for surge and heave motion are normalized by the mass of the fluid displaced by the body $\left(0.25\rho\right)$ and by $\left(0.25\rho a^2\right)$ for pitch motion.

Aspect Ratio:	Total Length:	Diameter at Center:	Water Depth:	Submergence:
6/1	*2a =2.38 [m]*	*2b =0.397 [m]*	*10 [m]*	*1 [m]*
5/1	*2a= 2.11 [m]*	*2b =0.422 [m]*	*10 [m]*	*1 [m]*
3/1	*2a =1.5 [m]*	*2b =0.50 [m]*	*10 [m]*	*1 [m]*

Table 6-2: Parameters of Hull 2 for Displaced Volume = 0.25 [m^3]

6.3.1 Hydrodynamic Coefficients in Linear Frequency Domain

In figures 6-14 to 6-19, the radiation coefficients for Hull 2 are presented for three degrees of freedom; surge, heave, and pitch. The *y*-axis of each plot is labeled with the parameters used to normalize the results.

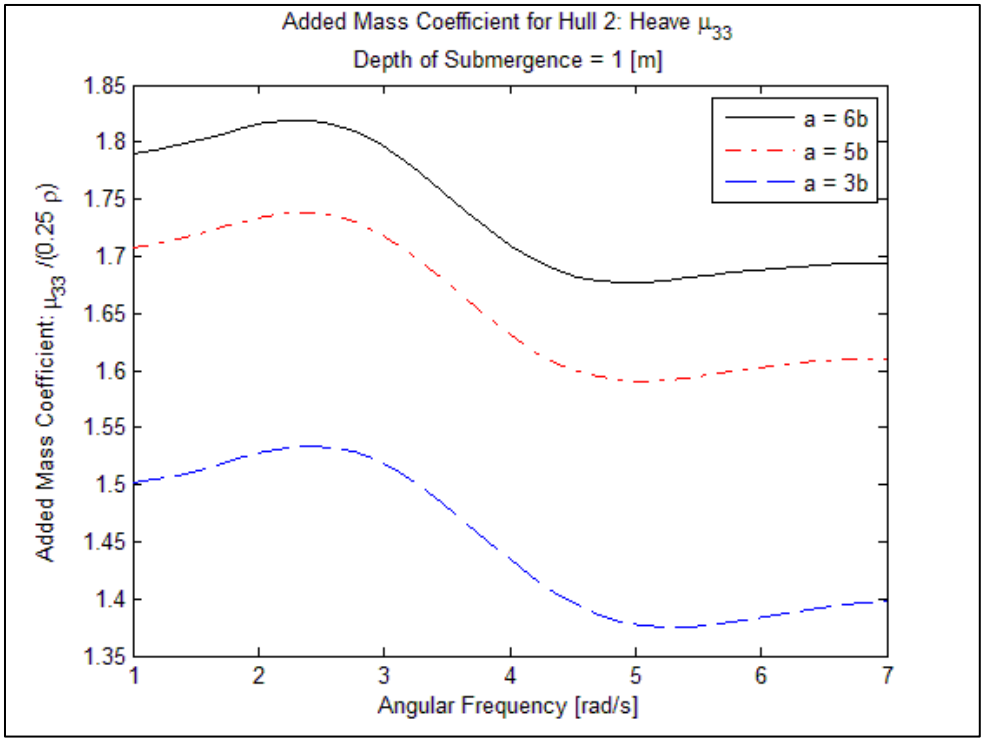

Figure 6-14: Added mass for Hull 2: Heave

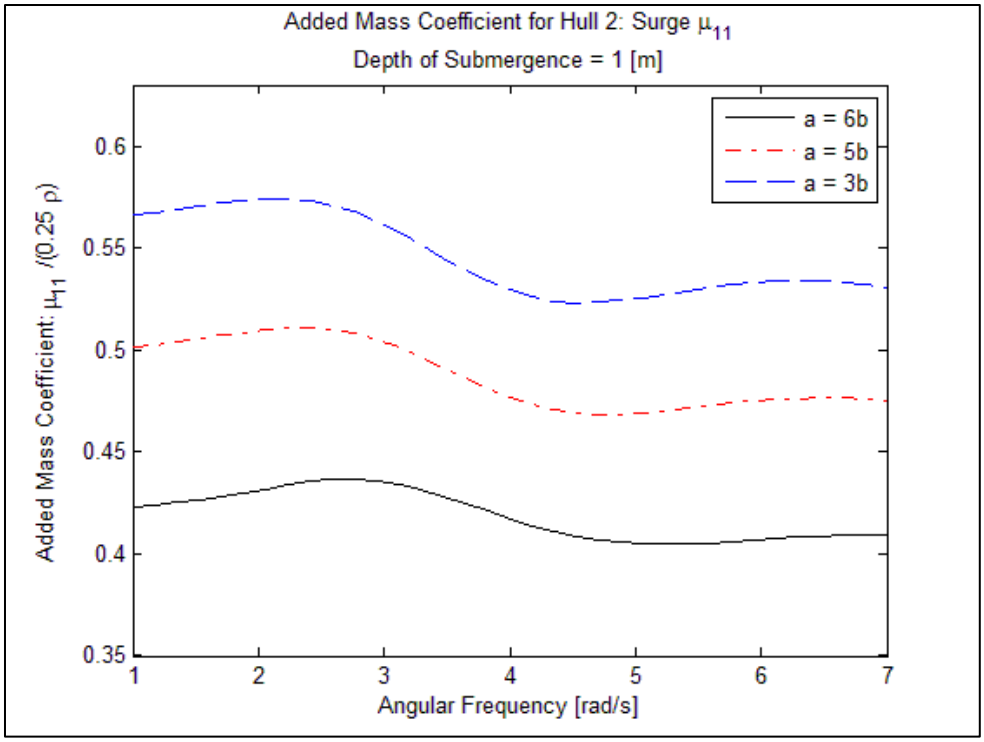

Figure 6-15: Added Mass for Hull 2: Surge

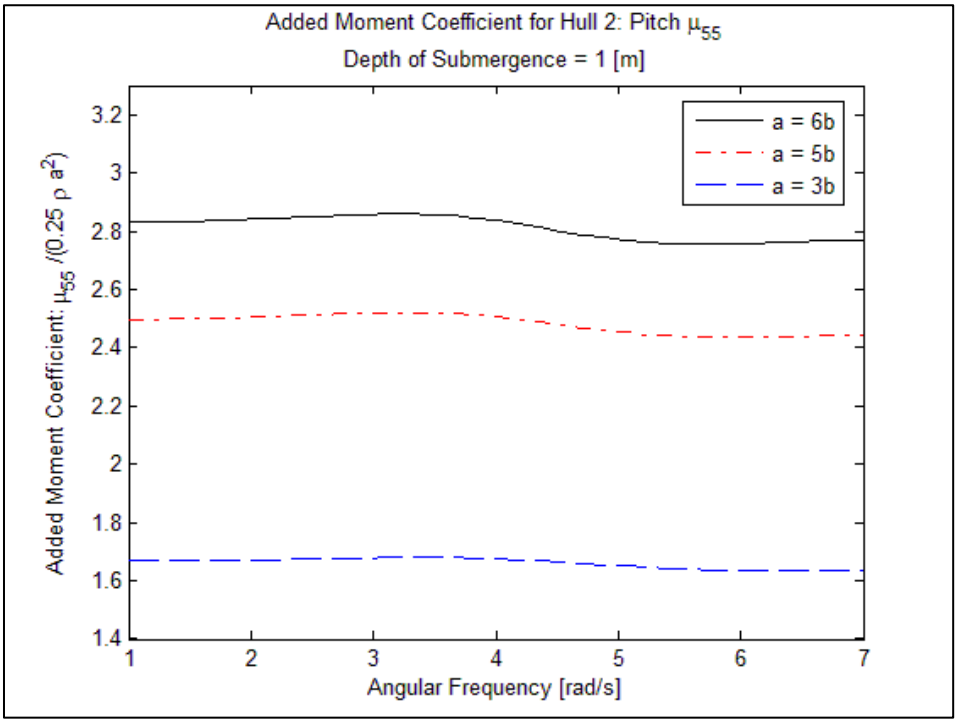

Figure 6-16: Added Moment of Inertia for Hull 2: Pitch

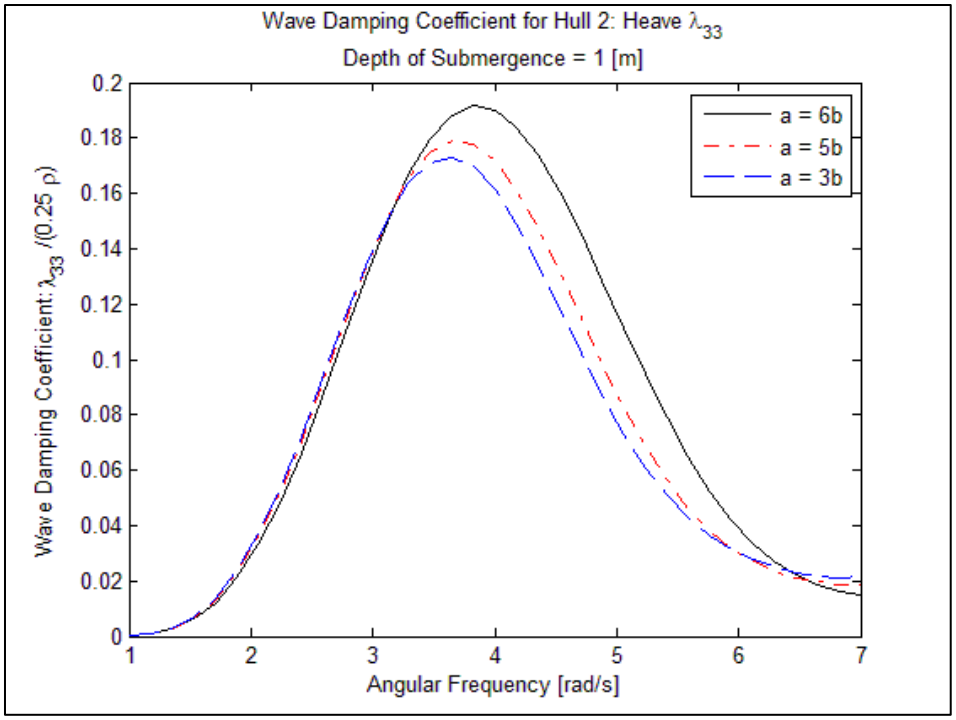

Figure 6-17: Wave damping for Hull 2: Heave

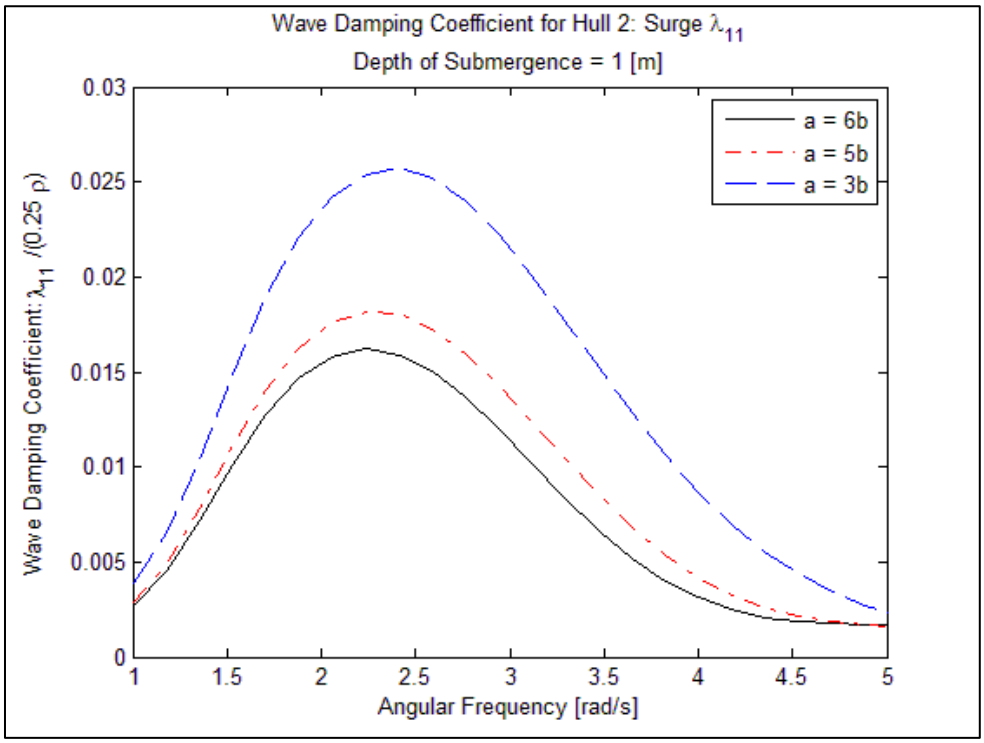

Figure 6-18: Wave Damping for Hull 2: Surge

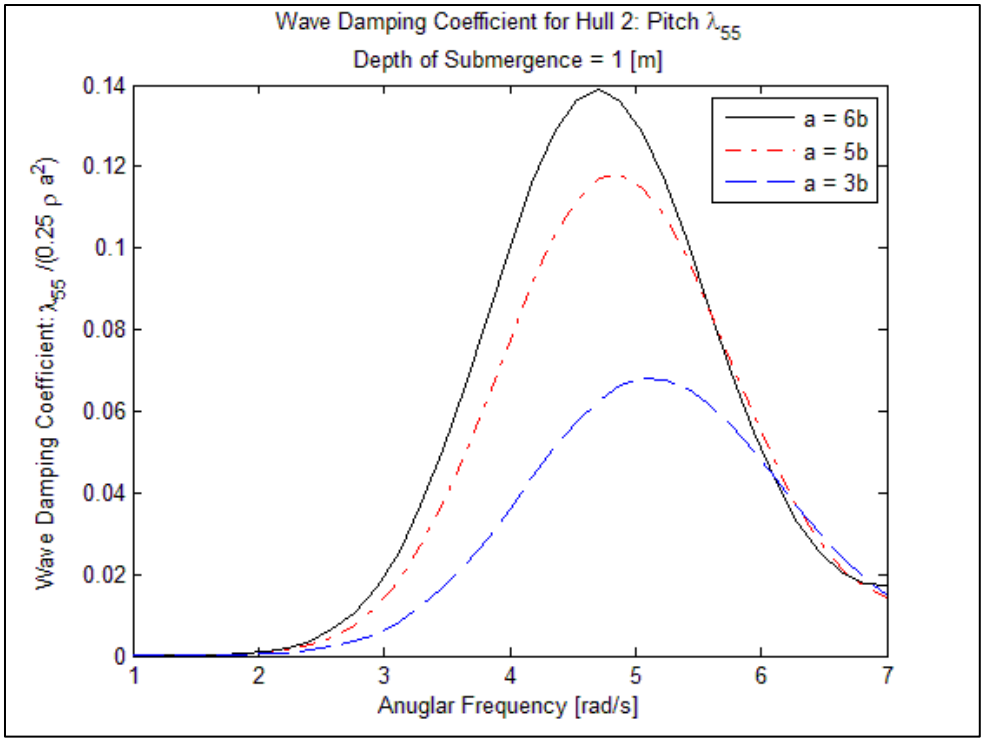

Figure 6-19: Wave Damping for Hull 2: Pitch

Figures 6-14 to 6-16 represent the added mass and moment coefficients for Hull 2 for surge, heave and pitch. For heave motion, the results show the highest added mass values for the body with the greatest overall length (*a = 6b*) which is consistent with the results found for Hull 1. Recall from table 6-2 that the longer body length is over 1.5 times longer than the shortest body length. This difference in length directly affects the added mass values for heave motion which is seen in figure 6-14. For surge motion, the broader aspect ratio of *a = 3b* has higher added mass values compared with the more slender bodies of *a = 6b* and *a = 5b* which is directly related to the surface area exposed in the *y-z* plane. This is clearly evident in figure 6-15. Figure 6-16 shows the added moment of inertia for pitch motion of Hull 2. Here, the higher added moment values are seen for the longer body length due to the greatest tip-to-center distance compared with the two shorter hull lengths.

Figures 6-17 to 6-19 show the wave damping coefficients for Hull 2 for surge, heave, and pitch. In the heave direction, the greatest damping coefficient values are associated with the longer body length (aspect ratio *a = 6b).* In Figure 6-17, note that at low frequencies, the wave damping is very similar for all aspect ratios but definitive differences become evident at the higher frequencies. The reason for that could be that as the oscillation rate increases, the body length effect also increases. These results show the longer body length with higher wave damping values at the peak frequency. For surge motion, the broad body creates higher wave damping values compared to the other bodies. However, opposite of what was seen for heave motion, the different aspect ratios have different wave damping values at low frequencies in the surge direction which shows that even at low frequencies, the body geometry influences the wave damping for surge motion. For pitch motion, the results show different wave damping values at low frequencies with the longer vehicle length having larger damping values at the peak frequency. At the higher frequency values the wave damping for all aspect ratios is very similar. The results suggest that the body geometry has little effect on heave damping at low frequency while at high frequency for surge and pitch.

6.3.2 Hull 2 Transfer Function in Frequency Domain

As done for Hull 1, the heave, surge and pitch motion transfer functions are determined using the radiating forces determined as above and wave exciting Froude-Krylov force.

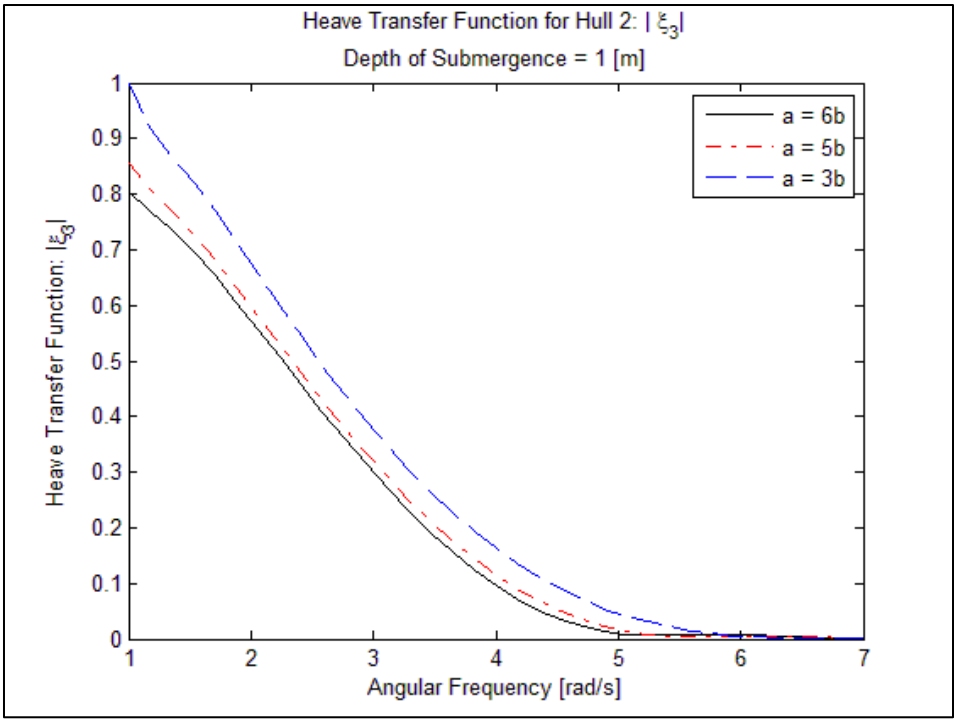

Figure 6-20: Heave Transfer Function for Hull 2

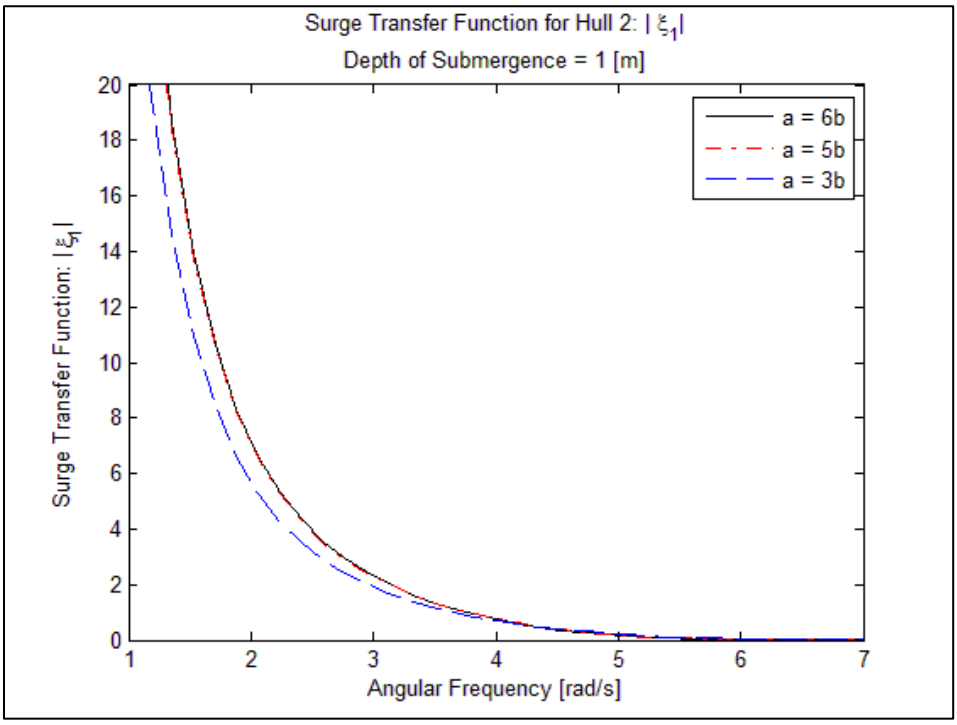

Figure 6-21: Surge Transfer Function for Hull 2

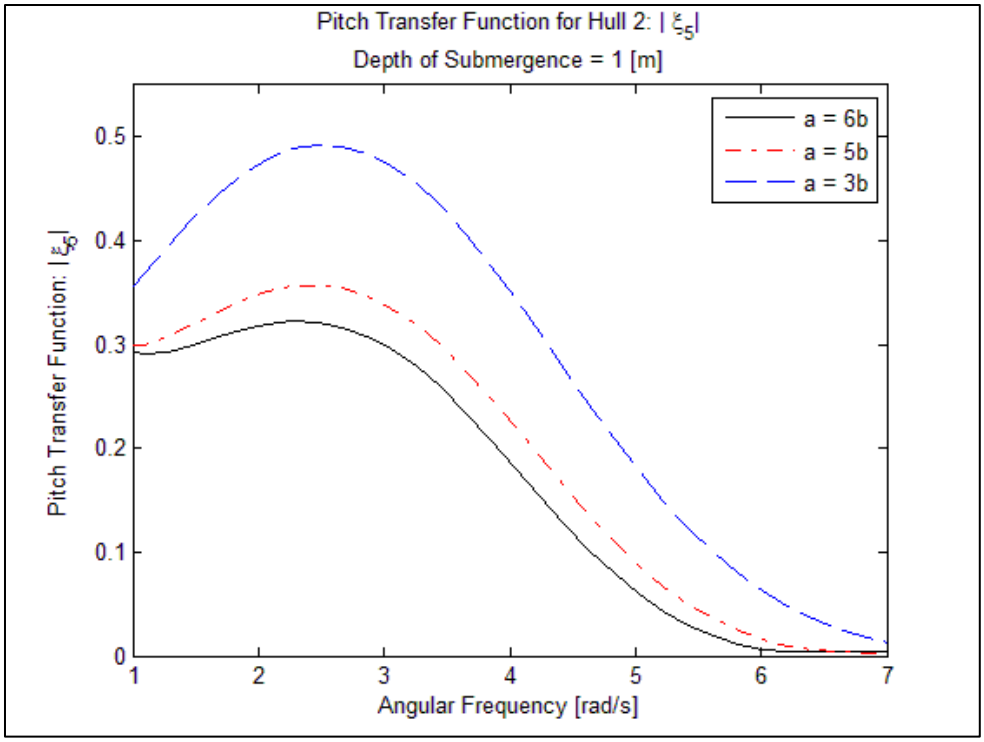

Figure 6-22: Pitch Transfer Function for Hull 2

Recall the discussion from section 6.2.2 about the restoring force of the submerged body in a homogenous fluid. Similarly for Hull 2, there is no restoring force for surge and heave motions and therefore the maximum responses are found at the lowest angular frequency. This explains the decreasing curve found for heave and surge motions. In figure 6-20, the results show the greatest response for the broad body of aspect ratio $a = 3b$. Figure 6-21 show very similar results for the different aspect ratios. In fact, the aspect ratios of $a = 6b$ and $a = 5b$ can be said to be the same. This result concludes that for surge motion in Hull 2, the body diameter has a low effect on the response. Recall that the pitch motion responses for both Hull 1 and Hull 2 create a restoring force and therefore the peak response is not at a frequency of 0 [rad/s] but instead at a higher angular frequency value as seen in figure 6-22. The metacentric height for Hull 2 was set the same as Hull 1 (GM= CG= 0.1a).

6.4 Results for Vehicle Submergence Depth of 2 Meters

The results presented in section 6.2 and 6.3 were representative of Hull 1 and Hull 2 for a vehicle submergence depth of 1 [m]. Additionally, more simulations were completed for a submergence depth of 2 [m]. These results are not shown in this report due to the vast amount of space needed to present the graphs. However, it can be concluded that as the vehicle submergence depth increases, the hydrodynamic coefficients, both added mass and wave damping, for Hull 1 and Hull 2 decrease as the effect from the surface is less as the vehicle distance from the surface increases. The difference is however smaller at low frequency which correspond long waves generated by the body motion. For this thesis, we focus on the minimizing the vehicle response in shallow waters with surface wave effects, therefore, the remaining results presented in this thesis utilize the hydrodynamic coefficients calculated for a submergence depth of 1 [m].

6.5 Comparison of Hull 1 and Hull 2

When comparing Hull 1 and Hull 2, one must take due caution. Although the body shapes maintain displacement between all aspect ratios, the body length and diameter change drastically between body shapes and aspect ratios. To show an example, the comparison of the hydrodynamic coefficients between Hull 1 aspect ratio 6/1 and Hull 2 aspect ratio 6/1 are shown in the following six figures. One will notice that for heave, surge, and pitch motions, Hull 2 has higher added mass and wave damping values compared to Hull 1.

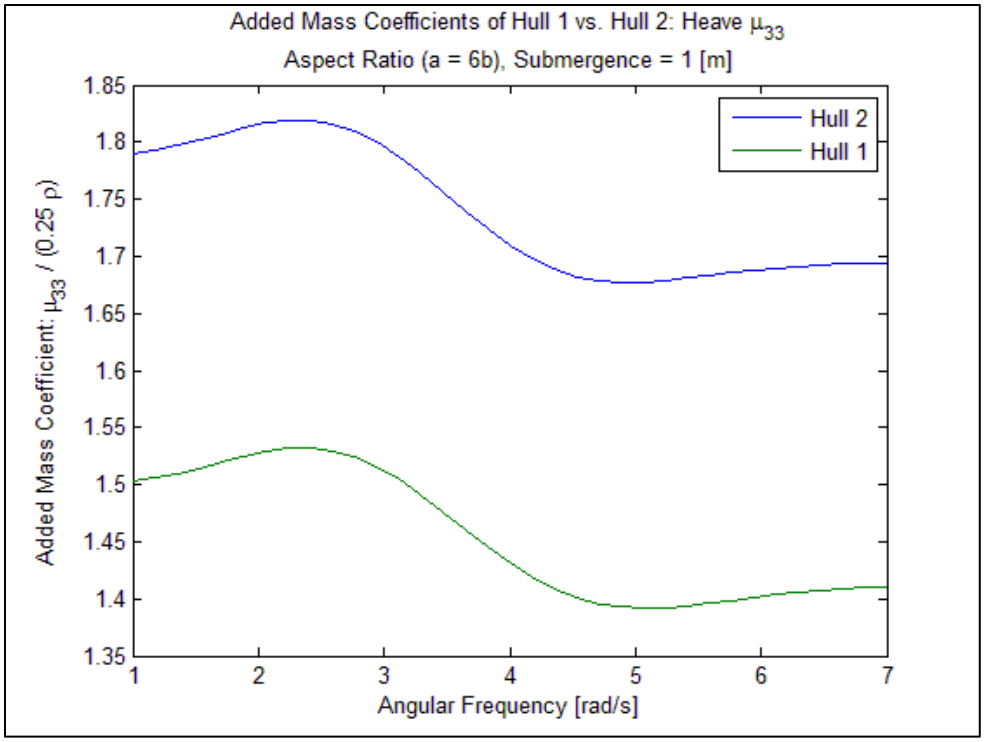

Figure 6-23: Added Mass Coefficient Hull 1 vs. Hull 2

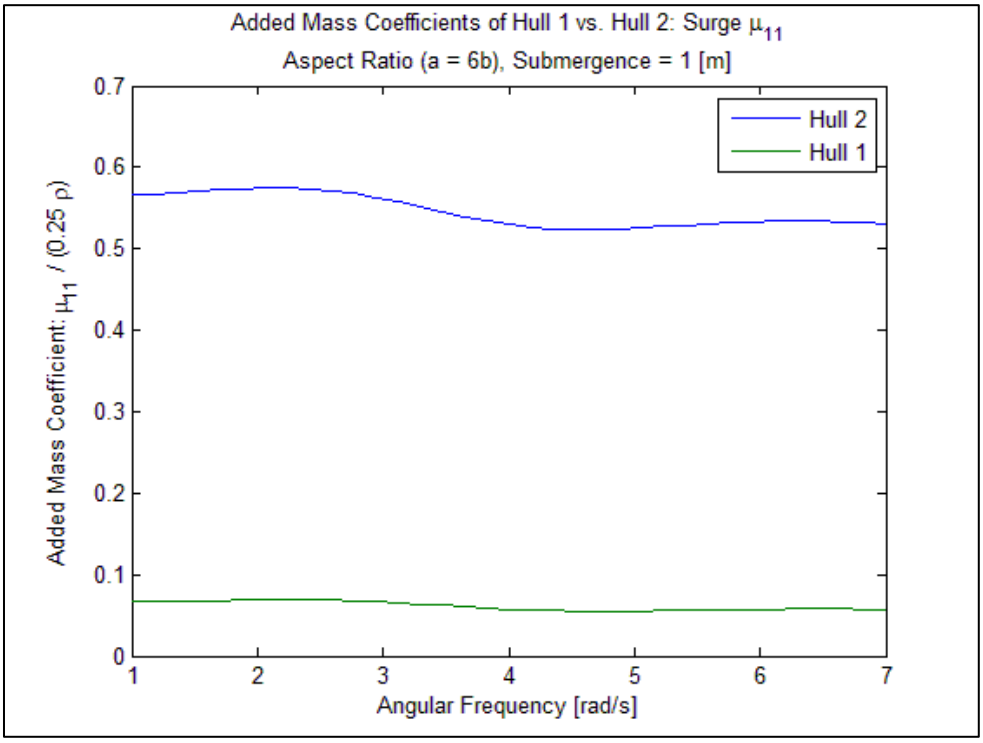

Figure 6-24: Surge Added Mass Coefficient Hull 1 vs. Hull 2

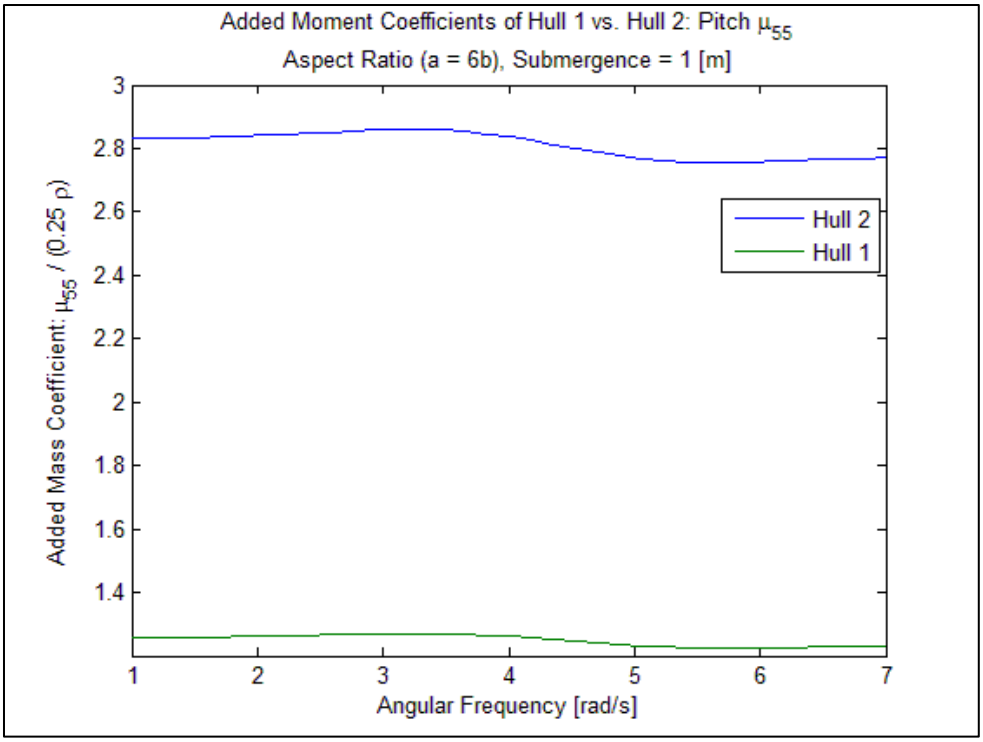

Figure 6-25: Pitch Added Moment Coefficient Hull 1 vs. Hull 2

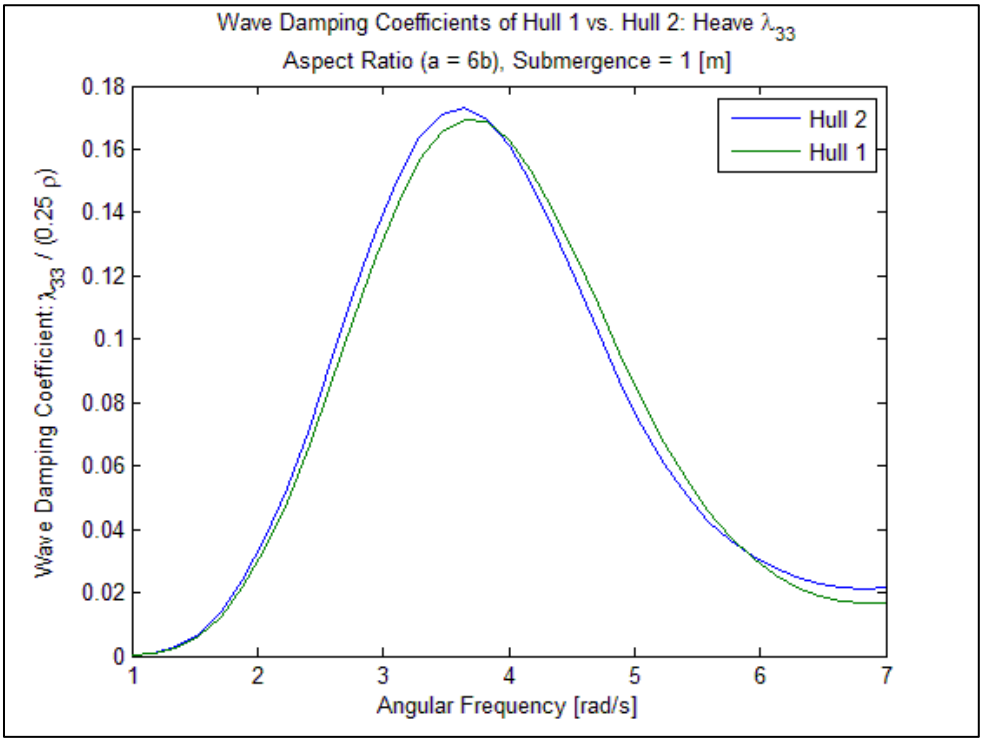

Figure 6-26: Heave Wave Damping Coefficients Hull 1 vs. Hull 2

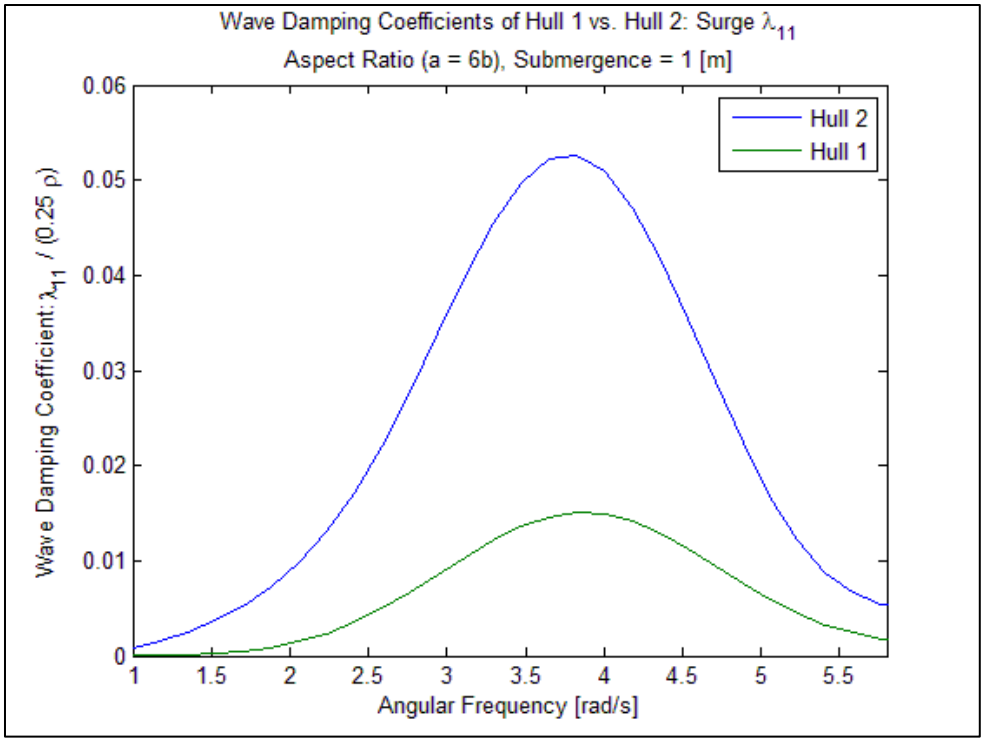

Figure 6-27: Surge Wave Damping Coefficients: Hull 1 vs. Hull 2

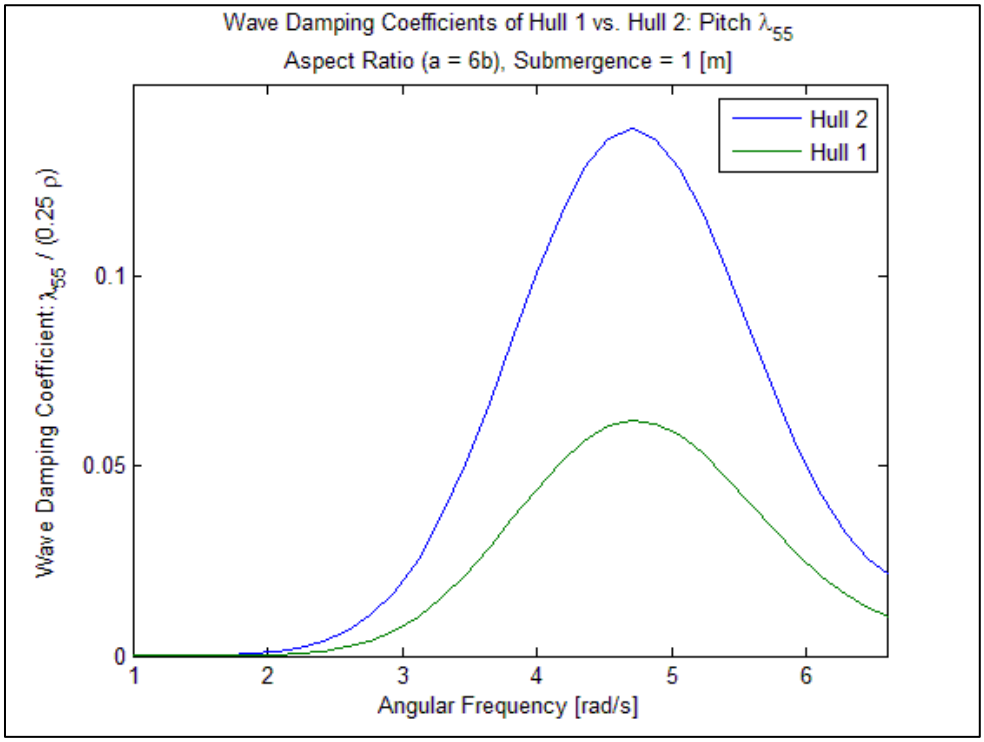

Figure 6-28: Pitch Wave Damping Coefficients Hull 1 vs. Hull 2

6.6 Response Spectrum

In this section, we join the transfer function with the TMA sea spectra to determine the response spectrum of the vehicle based on the geometry of the vehicle and the surface waves. To begin, we present different sea spectra for shallow waters near the coast for various wind speeds and fetch distances. The TMA wave spectrum has many input variables that can be changed for different geographic and weather scenarios. However, for this project, some variables will remain static namely, the incoming wave height will be held constant at 2 [m]. Additionally, the wave depth variable is set to 10 [m] as done for determination of the hydrodynamic coefficients. The remaining two variables which will remain dynamic are the wind speed and fetch, the distance between shore and the vehicle. In figures 6-29 and 6-30, a sample of the TMA spectra for various wind speeds and various fetch values are presented.

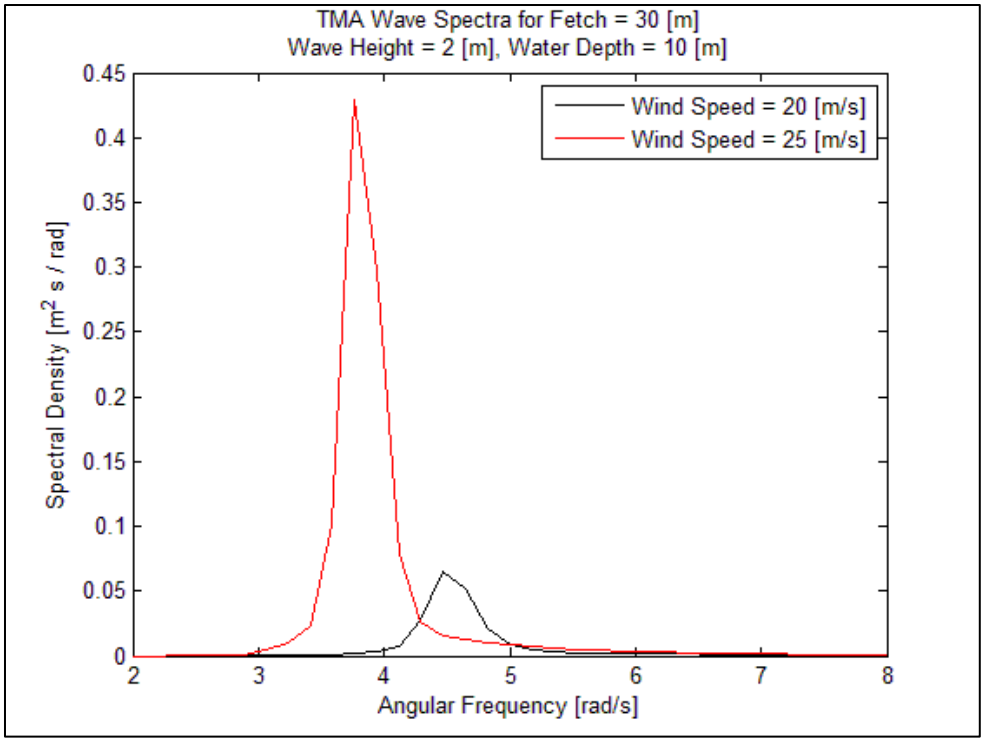

Figure 6-29: TMA Wave Spectra for Various Wind Speeds

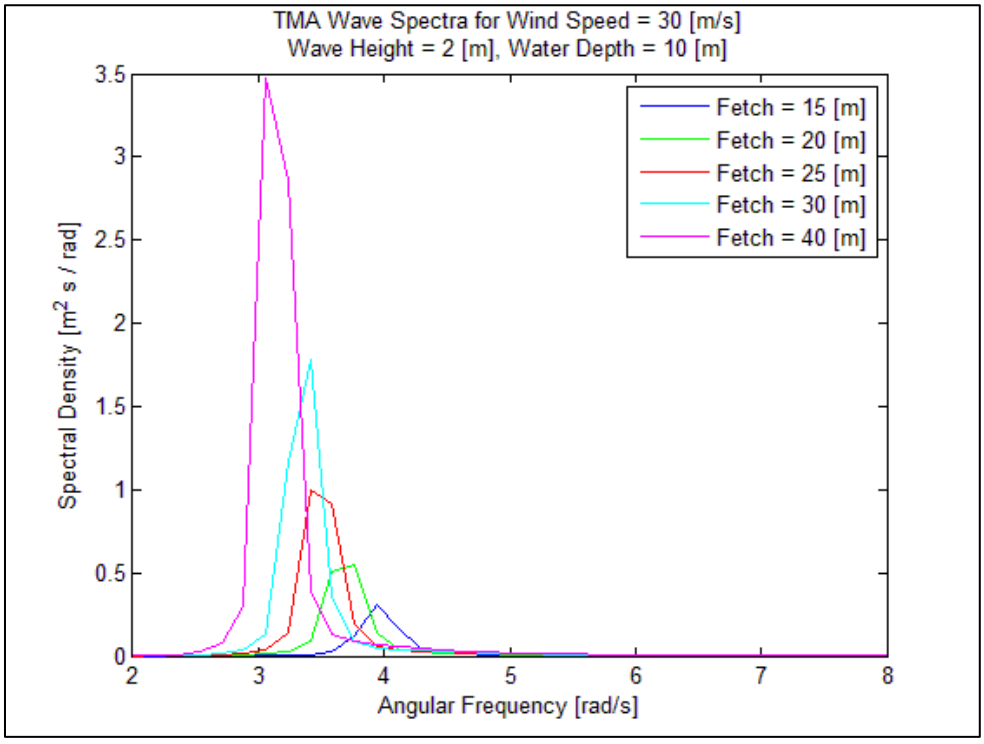

Figure 6-30: TMA Spectra for Various Fetch Values

In figure 6-29, it is apparent that the wind speed variable has a drastic effect on the spectral density values while in figure 6-30, changing the fetch distance does not change the amplitude of the spectral density as drastic as seen in the previous figure. The waves in these shallow areas close to shore are developed mostly by the wind and the water depth. Since the water depth remains constant, this explains why the change in wind speed has such a drastic effect. Increasing the fetch value allows more distance and time for the wave to build. Figure 6-30 shows that changing this distance does have an effect on the values but with an increment of 5 [m], the small increase in distance allows for the wave to build, but not drastically.

Next, we show the total response of the vehicle based on the geometric parameters and the wave spectra formulated based on wind speed and fetch.

6.6.1 Hull 1

The response spectrum was calculated for heave, surge, and pitch motions for all aspect ratios. Since one of the three aspect ratios was for a true sphere whose hydrodynamic pitch moment of inertia and damping are zero and cannot be compared to the other aspect ratios. Therefore, when analyzing the total response, the aspect ratio for a sphere ($a = b$) was omitted from pitch motion. Figures 6-31 through 6-33 present the response spectra for heave, surge, and pitch motions. With many combinations of input variables for the sea spectrum, one set of variable combinations is shown in these results representing one of many realistic sea conditions for waves considered near the shore. The input parameters chosen are as follows: water depth = 10 [m], wave height = 2 [m], fetch = 40 [m], and wind speed = 20 [m/s].

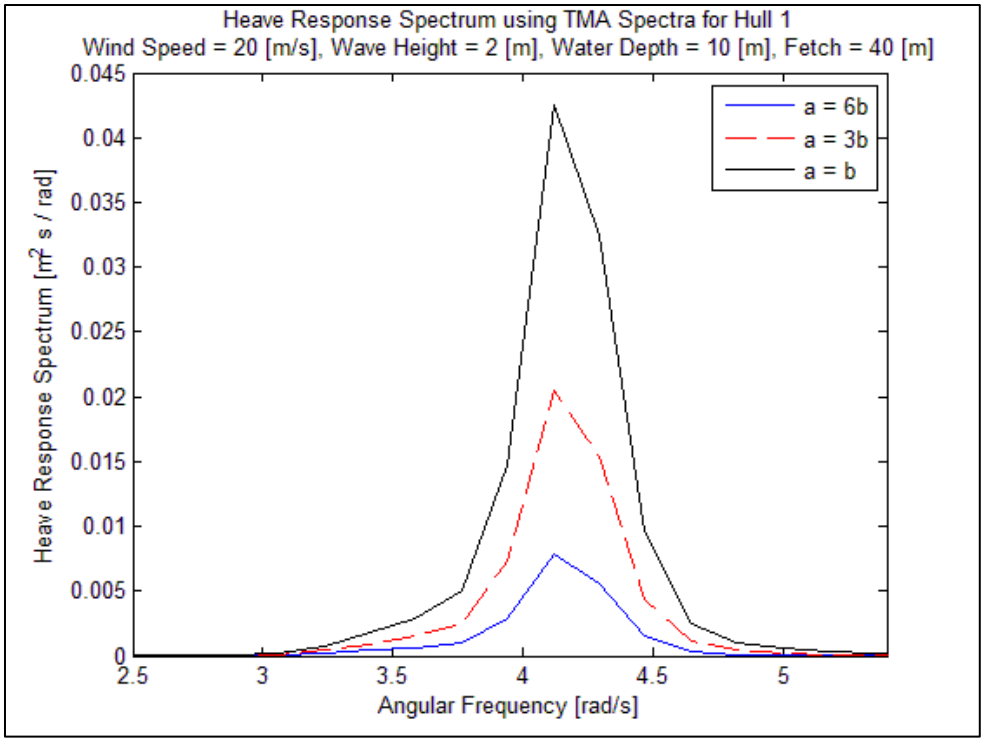

Figure 6-31: Response Spectrum for Hull 1: Heave

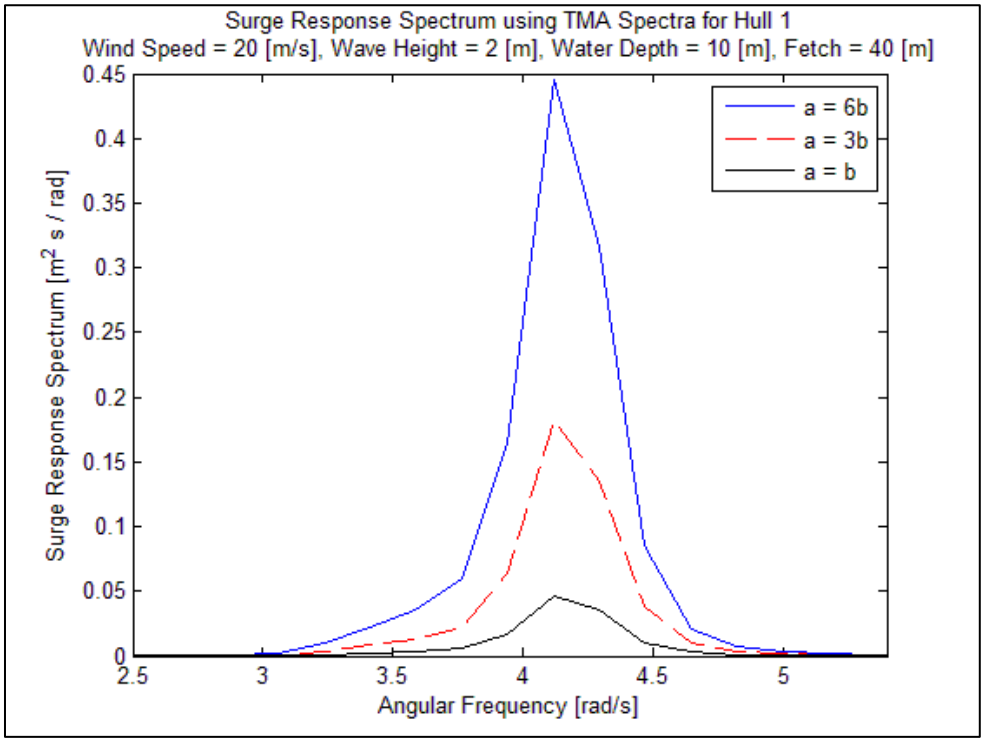

Figure 6-32: Response Spectrum for Hull 1: Surge

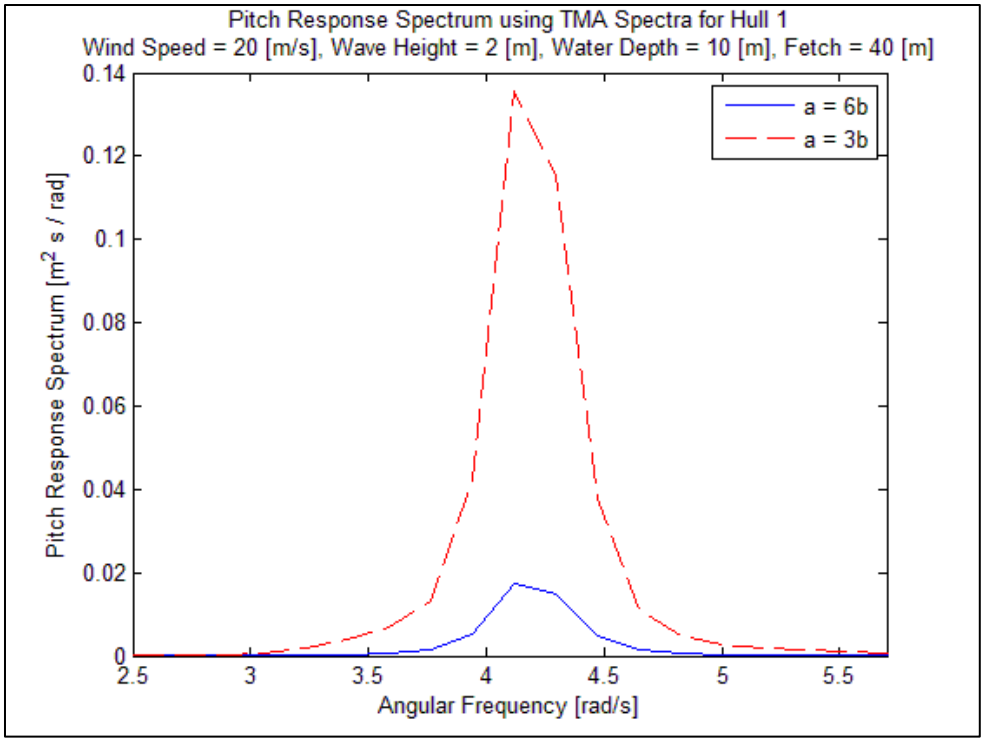

Figure 6-33: Response Spectrum for Hull 1: Pitch

For the above results, we refer to the aspect ratio of $a = 6b$ as the 'slender body' and the aspect ratio of $a = 3b$ as the 'bluff body' and $a = b$ as the 'sphere'. In figure 6-31, the body response for heave motion the sphere is about 10 times as much as the slender body. This is due to the longer body length overall for the more slender body. As for figure 6-32, the body response for surge motion is about ten times greater for the slender body compared with the sphere which is directly related to the body diameter. However, in figure 6-33, the body response for pitch motion is more than 7 times greater for the bluff body when compared to the slender. The increase in body length fore and aft creates less pitch response since there is a longer distance from the center of rotation to the end of the vehicle. For station keeping problems which is the focus of this project, a body with a large pitch response leads to poor station keeping characteristics and therefore can

say that the aspect ratio that minimizes the response is the slender, longer body (aspect ratio $a = 6b$).

In the next set of figures, we plot the response spectrum, TMA wave spectrum, the motion transfer function and the Froude-Krylov incident wave force for each mode of motion for Hull 1 aspect ratio ($a = 6b$). Recall from chapter 4 that the response spectrum is the product of the squared amplitude of the transfer function and the TMA wave spectrum. The response spectrum, TMA spectrum, transfer function and Froude-Krylov force were scaled in order to fit on the same graph. The legend in the top-right corner of the figure explains how each was scaled.

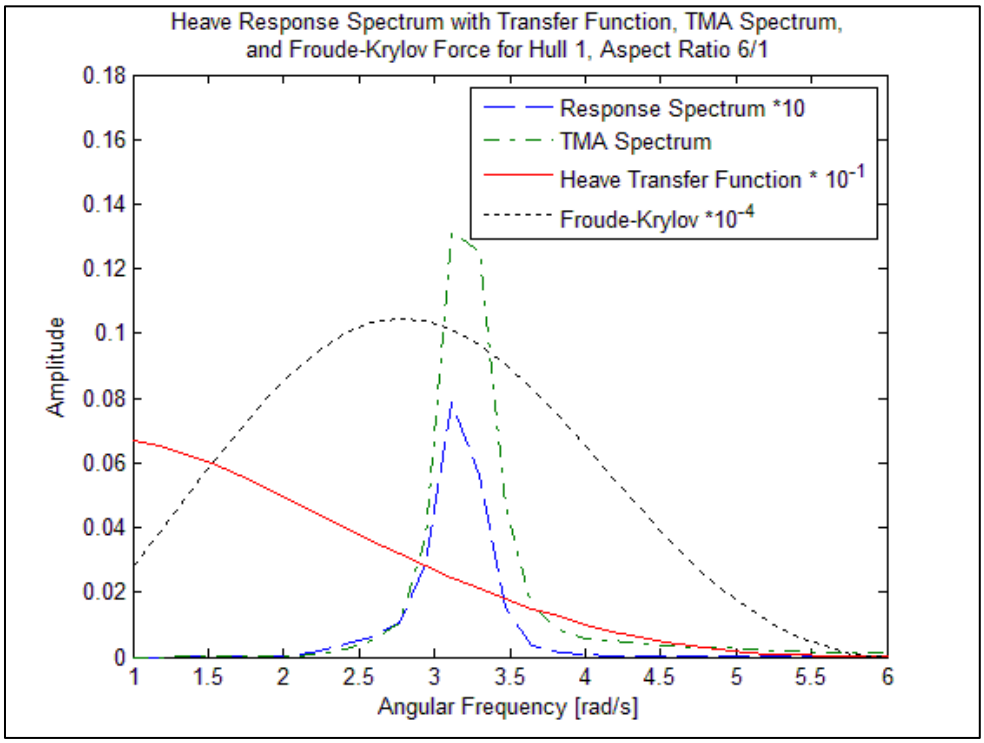

Figure 6-34: Heave Response Spectrum with Influence Variables

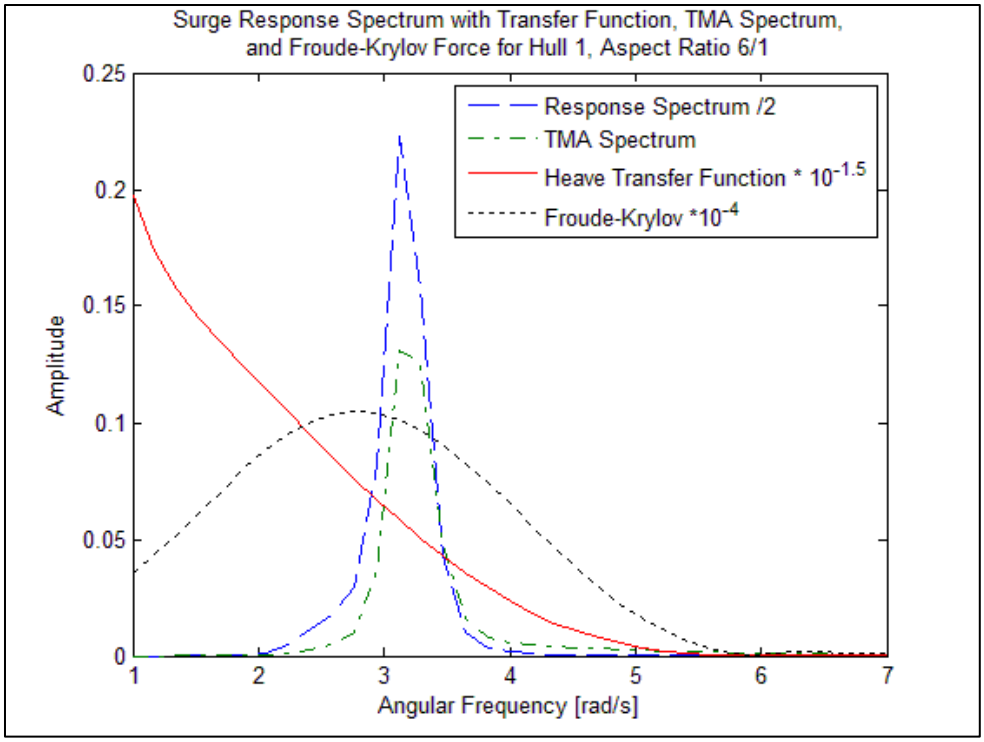

Figure 6-35: Surge Response Spectrum with Influence Variables

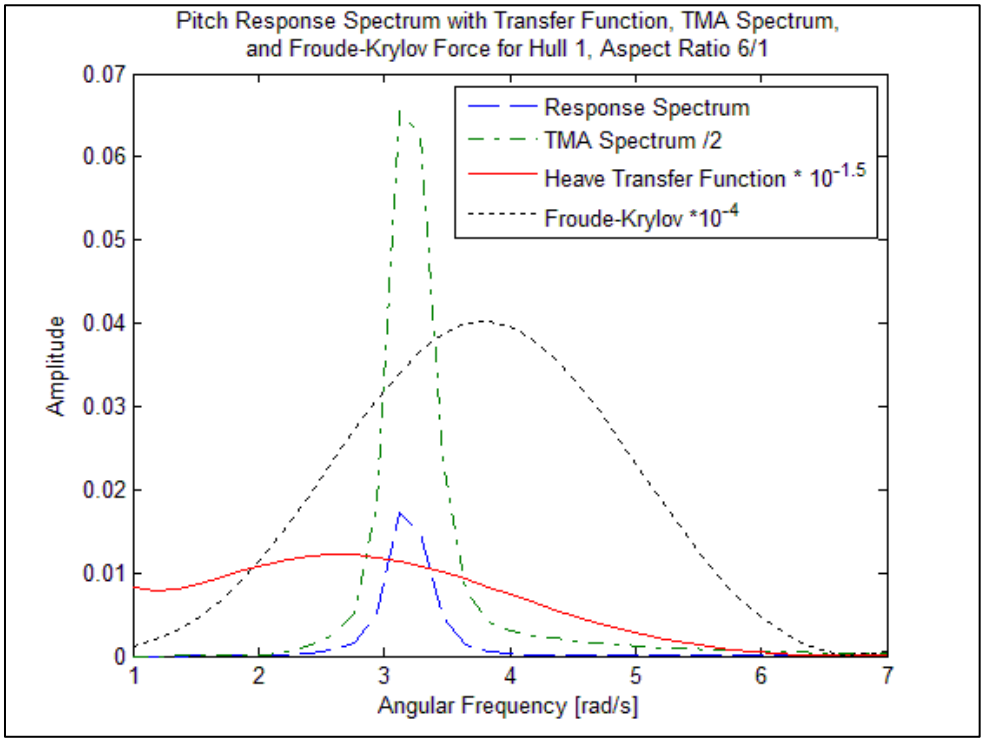

Figure 6-36: Pitch Response Spectrum with Influence Variables

6.6.2 Hull 2

Similarly in Hull 1, the total body response results are shown for the aspect ratios studied for heave, surge and pitch motions. To aid in comparison, the same sea spectra conditions used for Hull 1 were used again for Hull 2. Those parameters are as follows: water depth = 10 [m], wave height = 2 [m], fetch = 40 [m], and wind speed = 20 [m/s]. Figures 6-37 through 6-39 show these results.

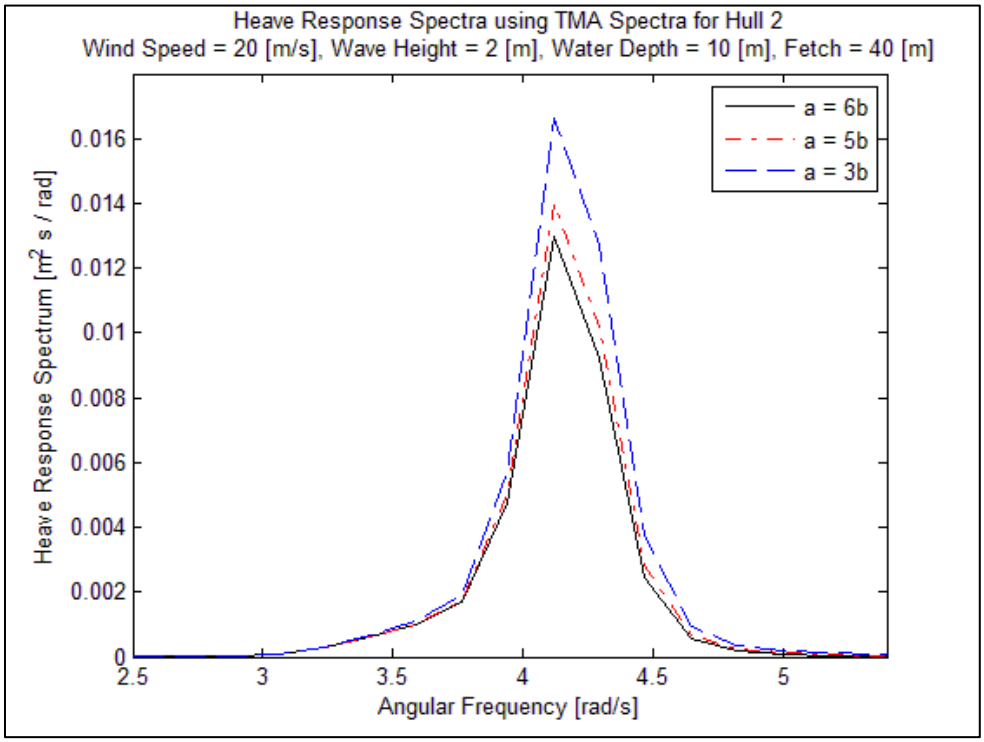

Figure 6-37: Response Spectrum for Hull 2: Heave

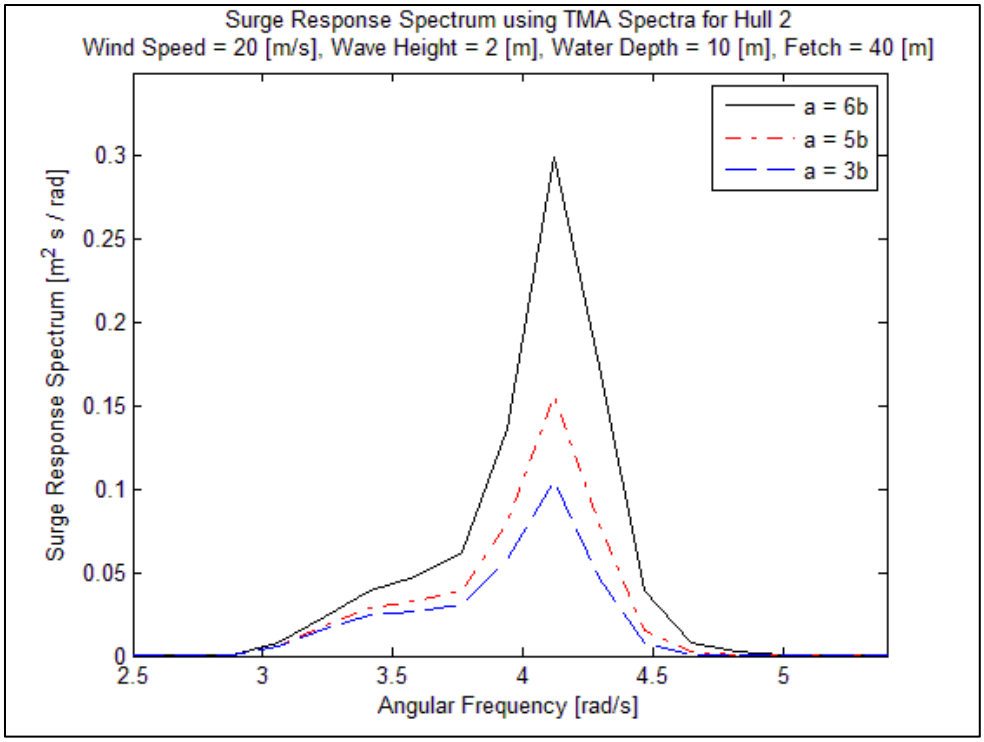

Figure 6-38: Response Spectrum for Hull 2: Surge

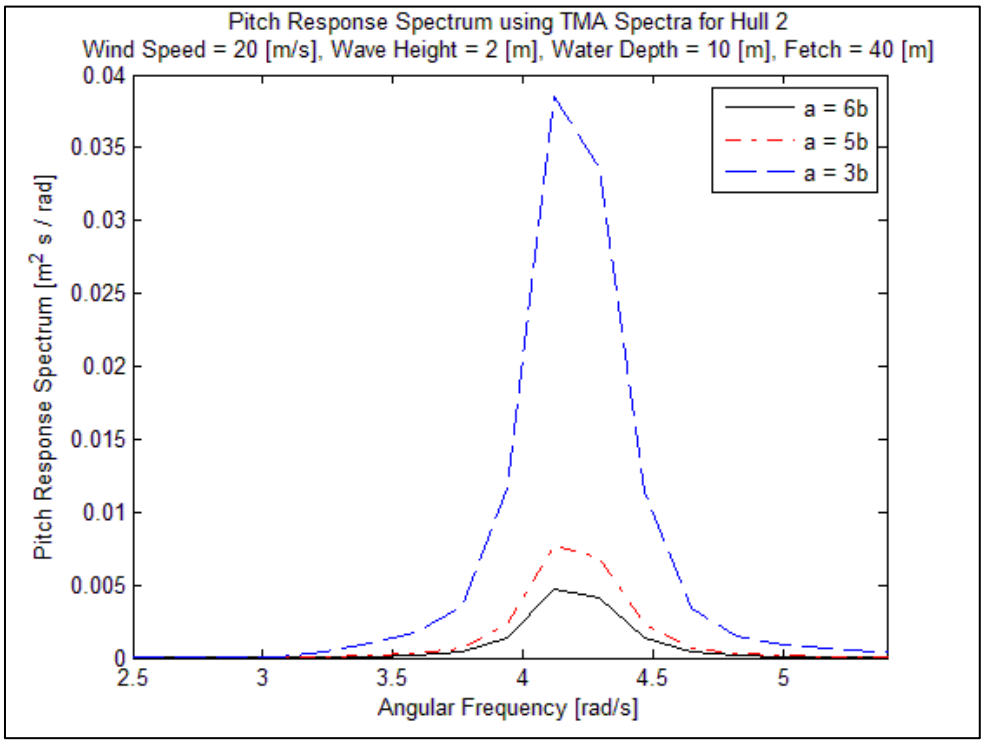

Figure 6-39: Response Spectrum for Hull 2: Pitch

For the Hull 2 results, we refer to the aspect ratio of $a = 6b$ as 'slender body', $a = 5b$ as 'intermediate body' and $a = 3b$ as 'bluff body'. In figure 6-37, the heave response results show the bluff body as having larger response compared to the other two aspect ratios. This result stems from the length of the body. Recall that in order to maintain a constant volume; the more slender body must have a longer body length. Figure 6-38 shows the surge amplitude response. Here, the slender body has larger amplitude compared to the other two aspect ratios. However, in both figures 6-37 and 6-38, the difference in amplitude between the slender body and broad body is about 1.3 times greater for heave and around 3 times greater for surge. As seen in Hull 1, the greatest difference between amplitude for the three aspect ratios is seen in the pitch response. Here, the bluff body response is about 8 times greater than the slender body. Again, this may be a factor of the body length as a longer body length (greater distance between center of rotation and end of the body) has a larger moment of inertia which minimizes the response of the vehicle. For Hull 2, the body aspect ratio which minimizes the body response is the again the longest body, aspect ratio of $a = 6b$.

In the next set of figures, we show the response spectrum for Hull 2 plotted with the TMA wave spectrum, the transfer function and the Froude-Krylov force for each mode of motion studied for the aspect ratio ($a = 6b$). Recall from chapter 4 that the response spectrum is the product of the squared amplitude of the transfer function and the TMA wave spectrum. The response spectrum, TMA spectrum, transfer function and Froude-Krylov force were scaled in order to fit on the same graph. The legend in the top-right corner of the figure explains how each was scaled.

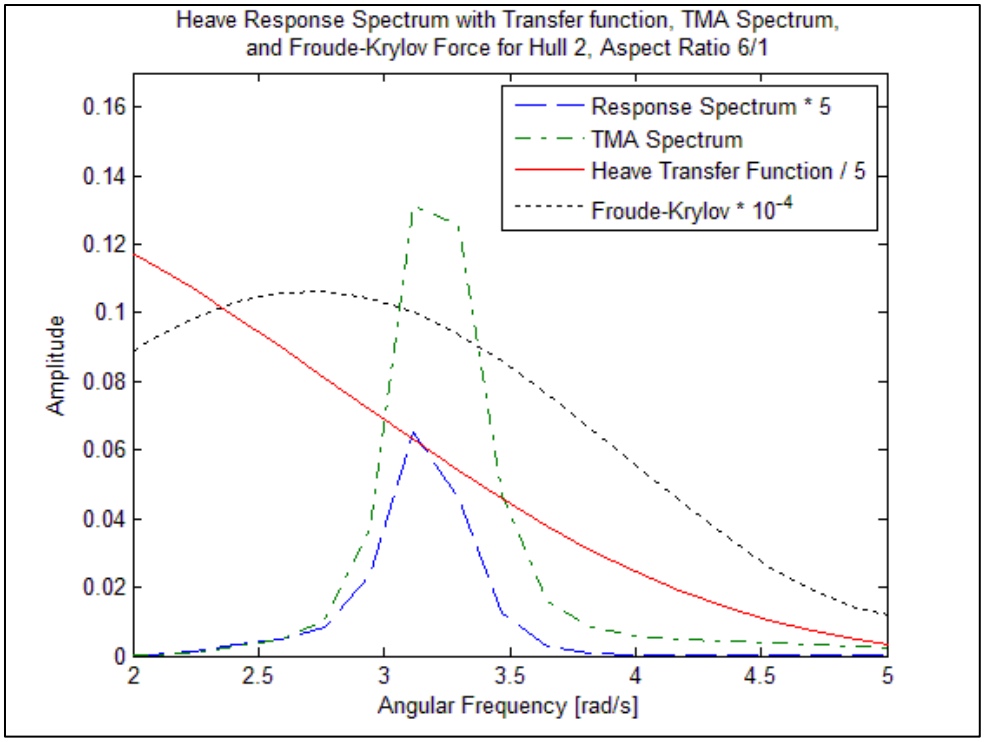

Figure 6-40: Heave Response Spectrum with Influence Variables

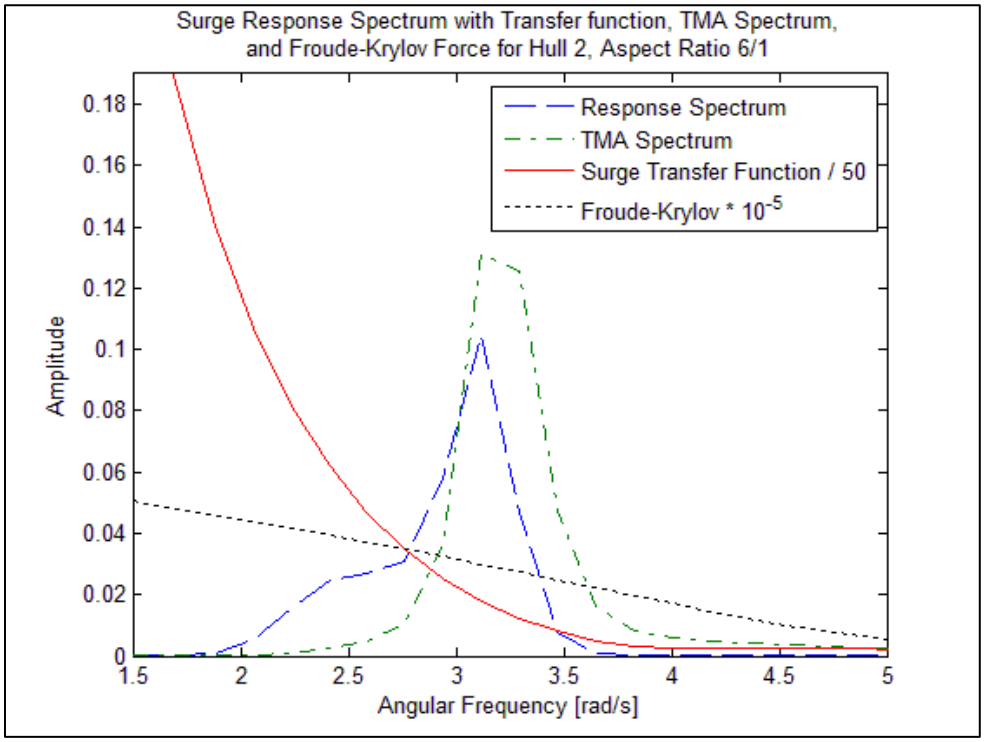

Figure 6-41: Surge Response Spectrum with Influence Variables

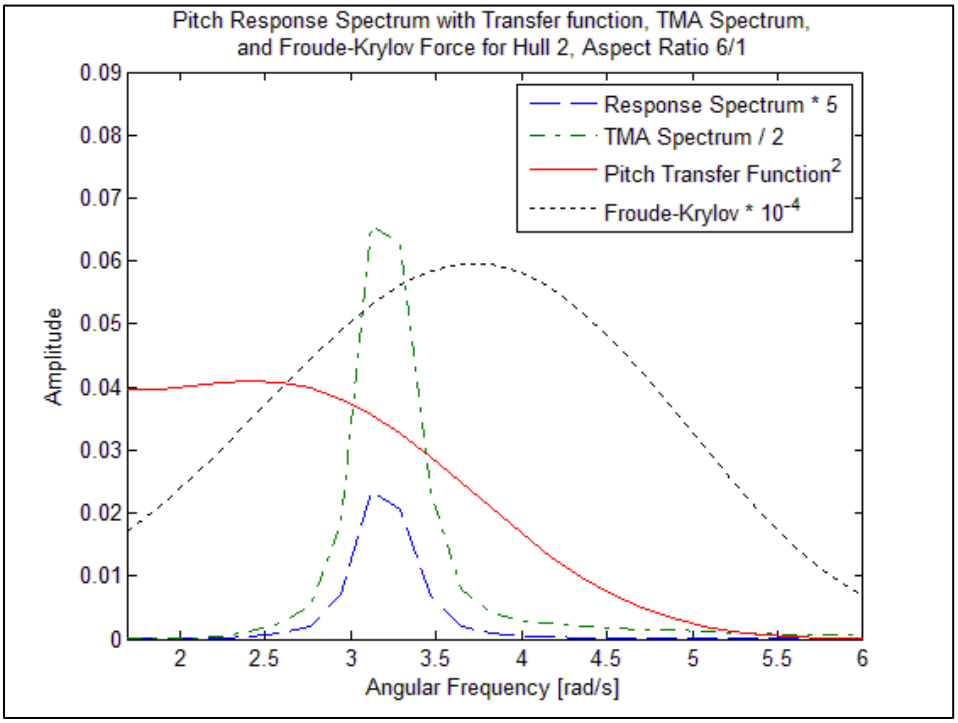

Figure 6-42: Pitch Response Spectrum with Influence Variables

CHAPTER 7: CONCLUSION

In the present thesis response characteristics of submerged bodies in shallow water wave fields was analyzed with the objective to determine body characteristics influencing wave exciting and wave radiation forces. For the frequency-domain analysis, a computational algorithm was developed using the boundary-integral method based on simple source distribution (Yeung [67]). Two series of hull shapes with one corresponding to prolate spheroid and the other to along parallel middle body with hemi-spherical nose section and conical tail section were considered in the present work. Heave, surge and pitch modes of motion were considered. Results of radiation force coefficients, transfer function and response spectra in shallow water waves were obtained for a range of hull aspect ratios, wave frequencies and hull submergence. TMA model relation was used to obtain the shallow water sea spectra for various wind speeds and fetch. Results show that the second hull shape with a large aspect ratio performed better, with regard to radiation forces, in heave and pitch modes compared to the first hull shape. The algorithm developed can be readily adapted to study the wave hydrodynamic characteristics of other hull shapes, e.g. oblate spheroid, batoid etc.

As future work, a time-domain nonlinear analysis can carried out using the mixed Eulerian-Lagrangian formulation of Longuet-Higgins and Cokelet [36] as outlined in Chapter 3 with corresponding numerical schemes given in Appendix C of the thesis.

Viscous flow analysis may be carried out particularly for low frequencies where viscous damping force may be important.

The numerical tool developed in the present can be also readily integrated in to design and vehicle control software.

APPENDIX A: NON-DIMENSIONALIZATION

In this appendix, the process for non-dimensionalization is presented. There were two procedures used to non-dimensionalize the parameters. The first procedure non-dimensionalized the parameters with respect to density (ρ), gravity (g) and body length (L). Examples are presented below

Denomination	Dimensional	Non-dimensional
Density	ρ	$\rho^* = \frac{\rho}{\rho} = 1$
Gravity	g	$g^* = \frac{g}{g} = 1$
Radius	L	$L^* = \frac{L}{L} = 1$
Coordinates	x,y,z	$x^* = \frac{x}{L}, y^* = \frac{y}{L}, z^* = \frac{z}{L}$
Angular frequency	σ	$\sigma^* = \sigma\sqrt{\frac{L}{g}}$
Pressure	p	$p^* = \frac{p}{\rho g L}$
Force	F	$F^* = \frac{F}{\rho g L^3}$
Velocity potential	ϕ	$\phi^* = \frac{\phi}{L\sqrt{gL}}$

The second procedure was used to present the hydrodynamic coefficients. This procedure divided the results by the mass of the fluid displaced by the body.

$$\mu_{ij}^{*} = \begin{cases} \dfrac{\mu_{ij}}{V\rho} & \text{for i = 1,2,3 and j = 1,2,3} \\ \dfrac{\mu_{ij}}{V\rho a^2} & \text{for i = 4,5,6 and j = 4,5,6} \\ \dfrac{\mu_{ij}}{V\rho a} & \text{otherwise} \end{cases}$$

where V is the vehicle volume. The wave damping is also non-dimensionalized in the same manner as the added mass. Therefore, the wave damping values actually have a dimension of [1/s]. The definitions are shown next.

$$\lambda_{ij}^{*} = \begin{cases} \dfrac{\lambda_{ij}}{V\rho} & \text{for i = 1,2,3 and j = 1,2,3} \\ \dfrac{\lambda_{ij}}{V\rho a^2} & \text{for i = 4,5,6 and j = 4,5,6} \\ \dfrac{\lambda_{ij}}{V\rho a} & \text{otherwise} \end{cases}$$

APPENDIX B: TMA WAVE SPECTRA

The TMA wave spectrum, as described in Chapter 4, is a modified JONSWAP spectra equation. It utilizes the variables found in the JONSWAP method but adds a depth limiting variable. Below, the TWA spectra equation is shown followed by the definitions and equations for each variable used.

$$S_{TMA} = \alpha g^2 \sigma^{-5} \kappa(\sigma, h) e^A$$

$$A = -\frac{5}{4}\left(\frac{\sigma_P}{\sigma}\right)^4 + \ln(\gamma) e^B$$

$$B = -\frac{1}{2}\left(\frac{\sigma - \sigma_P}{\omega(\sigma)\sigma_P}\right)^2$$

Where:

$$\kappa(\sigma,h)=\begin{cases}0.5\left(\sigma\sqrt{h/g}\right)^2 & \text{if } \sigma\sqrt{h/g}<1\\ 1-0.5\left(2-\sigma\sqrt{h/g}\right)^2 & \text{if } 1\le\sigma\sqrt{h/g}<2\\ 1 & \text{if } \sigma\sqrt{h/g}>2\end{cases}$$

σ = Angular Frequency

h = Water Depth

g = Gravity Constant

κ = Limited Depth Equation

α = Phillip's Constant

σ_P = Peak Angular Frequency

γ = Peak Enhancement Factor

ω = Standard Deviation

$$\omega=\begin{cases}0.07 \text{ if } \sigma<\sigma_P\\ 0.09 \text{ if } \sigma>\sigma_P\end{cases}$$

APPENDIX C: ITERATIVE SOLVERS

This appendix presents the higher order numerical schemes used to integrate the free surface conditions as used by others, example, Grosenbaugh and Yeung (1989). If higher order schemes are not used in the time domain, numerical instabilities may form and cause erroneous results. The two methods focused on with this thesis are the 4^{th} order Adams-Bashforth-Moulton scheme and the 4^{th} order Runge-Kutta scheme. In the remaining parts of this appendix, the details and application equations are derived.

B.1: 4^{th} Order Adams-Bashforth-Moulton scheme

This method is sometimes referred to as the Predictor-Corrector scheme as it uses a two-step process to update the free surface. In the predictor step, the solution from previous time iterations is updated using a numerical scheme. The corrector step then uses another numerical scheme to correct the solution from the predictor step. This method is only beneficial is it used as a 4^{th} order scheme. However, when the time simulation first starts off, lower order schemes must be used until four previous solutions exist to bring the scheme to 4^{th} order. Presented next are the predictor and corrector steps starting with a 2^{nd} order scheme and stopping at the 4^{th} order scheme. In these steps, consider Δt to be the time step, $f(\phi)$ to equal $\frac{\partial \phi}{\partial t}$ and ϕ to equal either ϕ or η depending on weather the surface elevation or surface potential is being updated.

2nd Order:

Predictor step: $\phi_P^{n+1} = \phi^n + \frac{\Delta t}{2}\left(3f\left(\phi^n\right) - f\left(\phi^{n-1}\right)\right)$

Corrector step: $\phi_c^{n+1} = \phi^n + \frac{\Delta t}{2}\left(f\left(\phi_P^{n+1}\right) + f\left(\phi^n\right)\right)$

3rd Order:

Predictor step: $\phi_P^{n+1} = \phi^n + \frac{\Delta t}{12}\left(23f\left(\phi^n\right) - 16f\left(\phi^{n-1}\right) + 5f\left(\phi^{n-2}\right)\right)$

Corrector step: $\phi_c^{n+1} = \phi^n + \frac{\Delta t}{12}\left(5f\left(\phi_p^{n+1}\right) + 8f\left(\phi^n\right) - f\left(\phi^{n-1}\right)\right)$

4th Order:

Predictor step: $\phi_p^{n+1} = \phi^n + \frac{\Delta t}{24}\left(55f\left(\phi^n\right) - 59f\left(\phi^{n-1}\right) + 37f\left(\phi^{n-2}\right) - 9f\left(\phi^{n-3}\right)\right)$

Corrector step: $\phi_c^{n+1} = \phi^n + \frac{\Delta t}{24}\left(9f\left(\phi_p^{n+1}\right) + 19f\left(\phi^n\right) - 5f\left(\phi^{n-1}\right) + f\left(\phi^{n-2}\right)\right)$

4th order Runge-Kutta Scheme:

This scheme is used commonly in the computational solution of partial differential equations. This method uses four steps instead of the two used in the Predictor-Corrector scheme. The details of this scheme are presented next. We consider a time iterative solution for the time step of $h = t_2 - t_1$ where $f\left(\phi\right)$ is equal to $\frac{\partial \phi}{\partial t}$ and ϕ to equal either ϕ or η depending on which free surface variable is being advanced.

1. Computer $f\left(\phi\right)$ at t_1

$$F_1\left(\phi_1, t_1\right) = \left.\frac{\partial \phi}{\partial t}\right|_{t=t_1}$$

2. Estimate ϕ at $t = t_1 + \frac{h}{2}$

$$\phi_{1+\frac{1}{2}} = \phi_1 + \frac{F_1 h}{2}$$

3. Compute $f(\phi)$ at $t = t_1 + h/2$

$$F_2\left(\phi_{1+1/2}, t_1 + h/2\right) = \left.\frac{\partial \phi}{\partial t}\right|_{t=t_1+h/2}$$

4. Correct ϕ at $t = t_1 + h/2$

$$\phi^c_{1+1/2} = \phi_1 + F_2 h/2$$

5. Correct $f(\phi)$ at $t = t_1 + h/2$

$$F_2\left(\phi^c_{1+1/2}, t_1 + h/2\right) = \left.\frac{\partial \phi}{\partial t}\right|_{t=t_1+h/2}$$

6. Estimate ϕ at $t = t_2$

$$\phi_2 = \phi_1 + F_2^c h/2$$

7. Compute $f(\phi)$ at $t = t_2$

$$F_3\left(\phi_2, t_2\right) = \left.\frac{\partial \phi}{\partial t}\right|_{t=t_2}$$

8. Correct ϕ at $t = t_2$

$$\phi_2^c = \phi_1 + \frac{h}{6}\left(F_1 + 2F_2 + 2F_2^c + F_3\right)$$

BIBLIOGRAPHY

[1] Abul-Azm, A.G., M. R. Gesraha. "Approximation to the Hydrodynamic of Floating Pontoons Under Oblique Waves." *Ocean Engineering* 27 (2000): 365-384. Print.

[2] Alben, Silas. "Simulating the Dynamics of Flexible Bodies and Vortex Sheets." *Journal of Computational Physics* 228 (2009): 2587-2603. Print.

[3] Alves, J., M. Banner, I. Young. "Revisiting the Pierson-Moskowitz Asymptotic Limits for Fully Developed Wind Waves. *Journal of Physical Oceanography* 33.7 (2003): 1301-1323. Print.

[4] Amromin, E. L., V Bushkovsky, V. Pashin. "Determination of Three-Dimensional Body Forms from Given Pressure Distribution Over Their Surfaces." *Journal of Ship Research.* 40.1 (1996): 22-27. Print.

[5] Ananthakrishnan, P., O. Saout. "Hydrodynamic and Dynamic Analysis to Determine the Directional Stability of an Underwater Vehicle Near a Free Surface." *Applied Ocean Research* 33 (2011): 158-167. Print.

[6] Ananthakrishnan, P. "Solution of nonlinear water-wave and wave-body interaction problems using a new boundary-fitted coordinates method." *Proceedings of the Fourth International Workshop on Water Waves and Floating Bodies."* Oystese, Norway (1990)

[7] Bose, Niel, Doug Perrault, Siu Young, Christopher Williams. "Sensitivity of AUV Added Mass Coefficients to Variations in Hull and Control Plane Geometry." *Ocean Engineering* 30 (2003): 645-671. Print.

[8] Cao, Yusong, William Shultz, and Robert Beck. "Three-Dimensional Desingularized Boundary Integral Methods for Potential Problems." *International Journal for Numerical Methods in Fluids* 12.8 (1991): 785-803. Print

[9] Chafin, Jesse. "Determination of Hydrodynamic Coefficients of Multi-Hill Ships For Seakeeping Analysis." M.S. Thesis. Florida Atlantic University. 2007.

[10] Chatjigeorgiou, Ioannis. "Hydrodynamic Exciting Forces on a Submerged Oblate Spheroid in Regular Waves." *Computers & Fluids* 57 (2012): 151-162. Print.

[11] Cho, I. H., M. H. Kim. "Wave Deformation by a Submerged Flexible Circular Disk." *Applied Ocean Research,* 21 (1991): 263-280. Print.

[12] Contento, Giorgio. "Numerical Wave Tank Computations of Nonlinear Motions of Two Dimensional Arbitrarily Shaped Free Floating Bodies." *Ocean Engineering* 17 (2000): 531-556. Print.

[13] Craik, Alex. "The Origins of Water Wave Theory." *Annual Review of Fluid Mechanics* 36 (2004): 1-28. Print

[14] Dalryample, Robert A, Robert G Dean. *Water Wave Mechanics for Engineers And Scientists.* Singapore: World Scientific, 1991. Print

[15] Duncan, W. J., A. S. Thom, A. D. Young. *Mechanics of Fluids.* New York: American Elsevier Publishing Company, Inc., 1960. Print.

[16] Edmong, Y., S. Tan, Z. Zhou. "Effect of Shallow and Narrow Water on Added Mass of Cylinders with Various Cross-Sectional Shapes." *Ocean Engineering* 32 (2005): 1199-1215. Print.

[17] *Encyclopedia of Physics*. 9. Fluid Dynamics III. Berlin: Springer-Verlag, 1960

[18] Fossen, Thor. *Guidance and Control of Ocean Vehicles.* New York: John Wiley & Sons. 1994. Print.

[19] Gomez-Gesteira, M., Dalrymple, R. "Using a Three-Dimensional Smoothed Particle Hydrodynamics Method for Wave Impact on a Tall Structure." *J. Waterway, Port, Coastal, Ocean Eng.,* 130(2), 2004: 63-69

[20] Grosenbaugh, M., R. Yeung. "Nonlinear Free-Surface Flow at a Two Dimensional Bow." *Journal of Fluid Mechanics* 209 (1989): 57-75. Print.

[21] Hirt, C. W., Nichols, B. D. "Volume of Fluid Method for the Dynamics of Free Boundaries." *Journal of Computational Physics* 39 (1981): 201-225

[22] Hughes, Steven. "The TMA Shallow-Water Spectrum Description and Applications." *Department of the Army: U.S. Army Corps of Engineers*. (1984). Print

[23] Hsu, John, Takumi Ohyama. "Nonlinear Wave Effect on the Slow Drift Motion of a Floating Body." *Applied Ocean Research* 17 (1995): 349-362. Print.

[24] Hu, Changhong, Xizeng Zhao. "Numerical and Experimental Study on a 2-D Floating Body Under Extreme Wave Conditions." *Applied Ocean Research* 35 (2012): 1-13. Print.

[25] Hu, Tianjiang, *et al.* "Computational Hydrodynamics and Statistical Modeling on Biologically Inspired Undulating Robotic Fins: A Two-Dimensional Study." *Journal of Bionic Engineering* 7 (2010): 66-76. Print.

[26] Hu, Tianjiang, Longxin Lin, Lincheng Shen, Haijun Xu. "Biological Inspirations, Kinematics Modeling, Mechanism Design and Experiments on an Undulating Robotic Fin Inspired by Gymnarchu nioloticus." *Mechanism and Machine Theory* 44 (2009): 633-645. Print.

[27] Jackson, J., Kenneth Lohmann, John Wang. "Perception of Wave Surge Motion By Hatchling Sea Turtles." *Journal of Experimental Marine Biology and Ecology* 229 (1998): 177-186. Print.

[28] Kawamata, Shigeru. "Effect of Wave-Induced Oscillatory Flow on Grazing by a Subtidal Sea Urchin Strongylocentrotus nudus." *Journal of Experimental Marine Biology and Ecology* 224 (1998): 31-48. Print.

[29] Kim, Taeyoung, Yonghwan Kim. "Numerical Analysis on Floating-Body Motion Responses in Arbitrary Bathymetry." *Ocean Engineering* 62 (2013): 123-139. Print.

[30] Kim, W. D., "On a Free-Floating Ship in Wave." *Journal of Ship Research* (September 1966): 182-191

[31] Korotkin, Alexandr I. *Added Masses of Ship Structures.* Russia: Springer, 2007. Print.

[32] Lee, C., J. Newman. "Solution of Radiating Problems With Exact Geometry." *16th Workshop on Water Waves and Floating Bodies – Hiroshima, Japan – 22-25, April 2001*

[33] Li, Gao-jin, Xi-yun Lu, Luodin Zhu. "Numerical Studies on Locomotion Performance of Fish-like Tail Fins." *Journal of Hydrodynamics* 24.4 (2012): 488-495. Print.

[34] Li, Y., Mian Lin. "Hydrodynamic Coefficients Induced by Waves and Currents For Submerged Circular Cylinder." *Procedia Engineering* 4 (2010): 253-261. Print.

[35] Linton, C. M. "Radiation and Diffraction of Water Waves by a Submerged Sphere in Finite Depth." *Ocean Engineering* 18.1 (1991): 61-74. Print.

[36] Longuet-Higgens, M., E. Cokelet. "The Deformation of Steep Surface Waves on Water: I. A Numerical Method of Computation." *Proceedings of Royal*

Society. 150 (1976): 1-26.

[37] Lopes, D, A. Sarmento. "Hydrodynamic Coefficients of a Submerged Pulsating Sphere In Finite Depth." *Ocean Engineering* 29 (2002): 1391-1398. Print.

[38] Low, K.H. "Modeling and Parametric Study of Modular Undulating Fin Rays for Fish Robots." *Mechanism and Machine Theory* 44 (2009): 615-632. Print.

[39] Lui, Yuming, Honhmei Yan. "An Efficient High-Order Boundary Element Method of Nonlinear Wave-Wave and Wave-Body Interactions." *Journal of Computational Physics* 230 (2011): 402-424. Print.

[40] Mei, Chiang C. *Mathematical Analysis in Engineering.* Cambridge: Cambridge University Press, 1997. Print.

[41] Michell, J. "The Wave Resistance of a Ship." *Philosophical Magazine* 45.272 (1898): 105-123.

[42] Miyata, H., Zhu, M., Watanabe, O. "Numerical Study on a Viscous Flow with Free-Surface Waves About a Ship in Steady Straight Course by a Finite Volume Method." *Journal of Ship Research* 36.4 (1992): 332-345

[43] Newman, J.N. *Marine Hydrodynamics.* Cambridge: The MIT Press, 1977. Print

[44] Ohkusu, M. "Hydrodynamics of Ships in Waves." *Advances in Marine Hydrodynamics.* Okhusu, M. Southampton: Computational Mechanics Publications, 1996. 77-132. Print

[45] Pedley, Timothy, Kiran Singh. "The Hydrodynamics of flexible-body maneuvers In Swimming Fish." *Physica D* 237 (2008): 2234-2239. Print.

[46] Pickard, George, Stephen Pond. *Introductory Dynamical Oceanography.* 2nd ed. Oxford: Elsevier Ltd., 1983. Print.

[47] Power, H, L.C. Wrobel. *Boundary Integral Methods in Fluid Mechanics.* Southampton: Computational Mechanics Publications, 1995. Print.

[48] Puaut, C. "Hydrodynamic Analysis of an Underwater Body including Free Surface Effects." M.S. Thesis. Florida Atlantic University, 2001.

[49] Rahman, Matiur. "Effects of Diffraction and Radiation on a Submerged Sphere." *International Journal of Mathematics and Mathematical Sciences* 28.9 (2001): 499-515. Print.

[50] Randall, Robert E. *Elements of Ocean Engineering.* New York: The Society of

Naval Architects and Marine Engineers, 2010. Print.

[51] Riedel, J.S. "Shallow Water Station Keeping of an Autonomous Underwater Vehicle: The Experimental Results of a Disturbance Compensation Controller," *OCEANS MTS/IEEE Conference and Exhibition* 2 (2000): 1017 1028. Print.

[52] Saout, Olivier. "Computation of Hydrodynamic Coefficients and Determination Of Dynamic Stability Characteristics of an Underwater Vehicle Including Free Surface Effects." M.S. Thesis. Florida Atlantic University. 2003.

[53] Takagi, T., *et al.* "Functional Morphology of the Flounder Allows Stable and Efficient Gliding: An Integrated Analysis of Swimming Behavior." *Aquatic Biology* 9.2 (2010): 149-153. Print.

[54] Taylor, R., G. Wu. "On the Radiation and Diffraction of Surface Waves by Submerged Spheroids." *Journal of Ship Research* 33 (1989): 84-92

[55] The Society of Naval Architects and Marine Engineers. *Principles of Naval Architecture.* New York: The Society of Naval Architects and Marine Engineers, 1967. Print.

[56] Tuck, O. "Ship-Hydrodynamic Free-Surface Problems Without Waves." *Journal of Ship Research* 35.4 (1991): 277-287. Print.

[57] Tuck, E., Vanden-Broeck, J. "Wave-less Free-Surface Pressure Distributions." *Journal of Ship Research.* 29 (1985): 151-158

[58] Tupper, Eric. *Introduction to Naval Architecture.* Oxford: Butterworth Heinemann, 1975. Print

[59] United States. Department of the Navy. *Shape Optimization in Free Surface Potential Flow Using an Adjoint Formulation.* Carderock, 2003. Print.

[60] Urabe, Minoru. *Nonlinear Autonomous Oscillations.* New York: Academic Press, 1967. Print.

[61] Ursell, F. "On the Heaving Motion of a Circular Cylinder on the Surface of a Fluid." *The Quarterly Journal of Mechanics and Applied Mathematics.* 2 (1949): 218-231

[62] Vogt, Mathias., Kang, Kuk-Jin. "A level set technique for computing 2D free surface flows." *International Workshop on Water Waves and Floating Bodies.* 12: (1997)

[63] Wang, G.M. “Kinematic Modeling and Dynamic Analysis of the Long-Based Undulation Fin of Gymnarchu niloticus.” *From Animals to Animats 9, Proceedings* 4095 (2006): 162-173. Print.

[64] Wehausen, John. *The Motion of Floating Bodies.* Annual Reviews, 1971. Print.

[65] Wehausen, John. “The Wave Resistance of Ships.” *Advances in Applied Mechanics* 13 (1973): 93-245. Print.

[66] Yeung, R. W. “Nonlinear Bow and Stern Waves – Inviscid and Viscous Solutions.” *Society for Industrial and Applied Mathematics* (1991): 349-369. Print.

[67] Yeung R.W. “A Singularity-Distribution Method for Free-Surface Flow Problems with an Oscillating Body.” Ph.D. Dissertation. University of California, Berkely, 1973.